ANGULAR MOMENTUM TRANSPORT BY MAGNETOHYDRODYNAMIC TURBULENCE IN ACCRETION DISKS: GAS PRESSURE DEPENDENCE OF THE SATURATION LEVEL OF THE MAGNETOROTATIONAL INSTABILITY

Takayoshi Sano,[1,2] Shu-ichiro Inutsuka,[3] Neal J. Turner,[4,5] and James M. Stone[1,6]

ABSTRACT

The saturation level of the magnetorotational instability (MRI) is investigated using three-dimensional MHD simulations. The shearing box approximation is adopted and the vertical component of gravity is ignored, so that the evolution of the MRI is followed in a small local part of the disk. We focus on the dependence of the saturation level of the stress on the gas pressure, which is a key assumption in the standard α disk model. From our numerical experiments we find that there is a weak power-law relation between the saturation level of the Maxwell stress and the gas pressure in the nonlinear regime; the higher the gas pressure, the larger the stress. Although the power-law index depends slightly on the initial field geometry, the relationship between stress and gas pressure is independent of the initial field strength and is unaffected by ohmic dissipation if the magnetic Reynolds number is at least 10. The relationship is the same in adiabatic calculations, where pressure increases over time, and nearly isothermal calculations, where pressure varies little with time. Over the entire region of parameter space explored, turbulence driven by the MRI has many characteristic ratios such as that of the Maxwell stress to the magnetic pressure. We also find that the amplitudes of the spatial fluctuations in density and the time variability in the stress are characterized by the ratio of magnetic pressure to gas pressure in the nonlinear regime. Our numerical results are qualitatively consistent with an idea that the saturation level of the MRI is determined by a balance between the growth of the MRI and the dissipation of the field through reconnection. The quantitative interpretation of the pressure-stress relation, however, may require advances in the theoretical understanding of nonsteady magnetic reconnection.

Subject headings: accretion, accretion disks — diffusion — instabilities — MHD — turbulence

1. INTRODUCTION

Most existing models of accretion disks are based on the α-prescription of Shakura & Sunyaev (1973). In this picture, the physical nature of the accretion torque is unspecified, and the radial-azimuthal component of the stress tensor, $w_{r\phi}$, is assumed to be a constant, α, times the pressure. Angular momentum is supposed to be transported outward by an "anomalous viscosity." The viscosity required by observed evolution timescale is orders of magnitude greater than that resulting from ordinary molecular viscosity. Dimensional analysis suggests that the anomalous viscosity can be represented by $\alpha c_s H$, where c_s and H are the sound speed and the disk scale height, respectively. The advantage of this approach is that many of the uncertainties regarding the accretion stress are confined in the single parameter α.

A promising physical mechanism for anomalous viscosity is turbulence. How turbulence might be driven has been an open question for many years. Keplerian disks satisfy Rayleigh's hydrodynamical stability criterion, as the specific angular momentum increases monotonically outward. No clear means for locally generating and sustaining hydrodynamic turbulence has been identified. When a magnetic field is present, however, the condition for stability is that the angular velocity Ω increases outward (Chandrasekhar 1961). This condition is usually violated in accretion disks. The presence of a weak magnetic field leads to magnetorotational instability (MRI; Balbus & Hawley 1991, 1998), which initiates and sustains MHD turbulence. Numerical simulations using several different methods have shown that Maxwell and Reynolds stresses in the turbulence transport a significant amount of angular momentum outward (e.g., Hawley, Gammie, & Balbus 1995, 1996; Matsumoto & Tajima 1995; Brandenburg et al. 1995). The Maxwell stress is a few times larger than the Reynolds stress.

In magnetized accretion disks, it is likely that the rate of angular momentum transport and the value of the α-parameter are determined by the saturation amplitude of the turbulence resulting from MRI. Numerical simulations indicate that the time- and volume-averaged Maxwell stress, $-B_r B_\phi/4\pi$, in the saturated state is usually proportional to the time- and volume-averaged magnetic pressure, $B^2/8\pi$ (e.g., Hawley et al. 1995, 1996). Therefore, it is important to determine how the magnetic pressure depends on the gas pressure, so that we can relate MHD calculations to the many existing studies that use the α-prescription. The magnetic pressure is controlled by generation and dissipation processes, and the rate of dissipation may vary with the gas pressure. The main aim of this work is to study how stress depends on gas pressure in turbulence driven by the MRI.

In the Shakura-Sunyaev picture, α is the ratio of the accretion stress to the gas pressure. The saturation level of the α parameter ranges from 10^{-3} to 0.1 in ideal MHD simulations

[1] Department of Applied Mathematics and Theoretical Physics, Centre for Mathematical Sciences, University of Cambridge, Wilberforce Road, Cambridge CB3 0WA, UK.

[2] Institute of Laser Engineering, Osaka University, Suita, Osaka 565-0871, Japan; sano@ile.osaka-u.ac.jp.

[3] Department of Physics, University of Kyoto, Kyoto 606-8502, Japan.

[4] Department of Physics, University of California, Santa Barbara, CA 93106-9530.

[5] Jet Propulsion Laboratory, California Institute of Technology, MS 169-506, 4800 Oak Grove Drive, Pasadena, CA 91109-8099.

[6] Department of Astrophysical Sciences, Princeton University, Peyton Hall, Princeton, NJ 08544-1001.

(e.g., Hawley et al. 1995, 1996). However, the important questions of how the MRI saturates and which physical quantities determine the saturation level have not yet been resolved. The ultimate goal of this work is to understand the mechanism of nonlinear saturation of the MRI, so that we can predict the saturation level from a small number of parameters. The first attempts to measure the parameter dependence of the stress numerically were made by Hawley et al. (1995, 1996). They found that the saturation level depends on the field strength, in disks penetrated by uniform vertical fields. On the other hand, the final state is independent of the initial field strength if there is no net magnetic flux in the system. A single initial gas pressure was used in all the calculations, so that the pressure dependence of the saturation level was not addressed. Here we extend the work of Hawley et al. (1995, 1996). We reexamine the predictor function, explicitly considering the pressure dependence. The calculations are run for hundreds of orbits for accurate estimation of saturation levels.

The gas pressure dependence of the saturated stress remains unclear. No numerical experiment has explicitly examined the dependence. However, there is indirect evidence that higher gas pressures may enhance the Maxwell stress. Stone et al. (1996) carried out three-dimensional simulations of the MRI in a vertically stratified disk using both adiabatic and isothermal equations of state. In the adiabatic case, temperatures increase with time as a result of dissipation of magnetic energy, while in the isothermal version, the temperature is constant. The pressures in the nonlinear regime differ substantially between the two. The saturation level in the adiabatic run is higher than in the isothermal run with the same initial condition, suggesting that higher pressures may contribute to higher saturation levels of the stress. However, the calculations include stratification, so that buoyancy, as well as gas pressure, may affect the saturated state. The effects of gas pressure are studied separately in the present paper using the unstratified shearing box approximation (Hawley et al. 1995).

Another advantage of unstratified local simulations is that the evolution can be followed for many orbits. Turbulence driven by the MRI is fluctuating and chaotic (Winters, Balbus, & Hawley 2003), and averages must be taken over long intervals for reliable estimates of the saturation level. Most of our simulations are integrated for a few hundred orbits, and time averages are taken over more than 50 orbits. These periods are long compared with previous work using similar calculations.

The plan of this paper is as follows. The basic equations and initial conditions are described in § 2. We make the local shearing box approximation, in which total energy increases over time because of the radial boundary conditions. Energy transfer and thermalization in the shearing box are also discussed briefly in § 2. Numerical results are shown in § 3. The parameters defining the initial condition in the local approximation are the gas pressure, the geometry and strength of the magnetic field, the equation of state, the size of the calculation box, and the numerical resolution. The effects of all parameters must be understood to construct a saturation predictor function. However, in this paper we concentrate on the gas pressure, magnetic field, and equation of state. The remaining parameters will be investigated in subsequent work. The evolution of the MRI in disks with zero and nonzero net magnetic flux is examined in §§ 3.1 and 3.2, respectively. The effects of magnetic dissipation are discussed in § 3.3, while § 3.4 is devoted to general characteristics of MHD turbulence driven by the MRI. Time variability of the turbulence and the interpretation of our numerical results are discussed in § 4. Finally, § 5 is a brief summary.

2. NUMERICAL METHOD

2.1. *Basic Equations and Numerical Scheme*

The shearing box approximation is used in our numerical simulations because we focus on the local behavior of the MRI in the simplest representation of accretion disks. The vertical gravity is ignored so that all the physical quantities are initially uniform except for the sheared velocity in the azimuthal direction. The equations to be solved are

$$\frac{\partial \rho}{\partial t} + \boldsymbol{v} \cdot \boldsymbol{\nabla} \rho = -\rho \boldsymbol{\nabla} \cdot \boldsymbol{v}, \tag{1}$$

$$\frac{\partial \boldsymbol{v}}{\partial t} + \boldsymbol{v} \cdot \boldsymbol{\nabla} \boldsymbol{v} = -\frac{\boldsymbol{\nabla} P}{\rho} + \frac{\boldsymbol{J} \times \boldsymbol{B}}{c\rho} - 2\boldsymbol{\Omega} \times \boldsymbol{v} + 2q\Omega^2 x\hat{\boldsymbol{x}}, \tag{2}$$

$$\frac{\partial \epsilon}{\partial t} + \boldsymbol{v} \cdot \boldsymbol{\nabla} \epsilon = -\frac{P\boldsymbol{\nabla} \cdot \boldsymbol{v}}{\rho} + \frac{4\pi \eta \boldsymbol{J}^2}{c^2 \rho}, \tag{3}$$

$$\frac{\partial \boldsymbol{B}}{\partial t} = \boldsymbol{\nabla} \times \left(\boldsymbol{v} \times \boldsymbol{B} - \frac{4\pi \eta \boldsymbol{J}}{c} \right), \tag{4}$$

where

$$\boldsymbol{J} = \frac{c}{4\pi} (\boldsymbol{\nabla} \times \boldsymbol{B}) \tag{5}$$

is the current density and ϵ is the specific internal energy. The basic equations are written in a local Cartesian frame of reference (x, y, z) corotating with the disk at angular frequency Ω, where x is oriented in the radial direction, y is in the azimuthal direction, and z is in the vertical direction. The terms $-2\boldsymbol{\Omega} \times \boldsymbol{v}$ and $2q\Omega^2 x$ in the equation of motion given by equation (2) are the Coriolis force and the tidal expansion of the effective potential with a constant $q = 3/2$ for a Keplerian disk, respectively. The gas is assumed to be ideal, with pressure $P = (\gamma - 1)\rho\epsilon$, where γ is the ratio of the specific heats. In this paper we examine both the ideal MHD and resistive MHD cases. The induction equation (4) includes a term for the ohmic dissipation, where η is the magnetic diffusivity. The energy equation (3) has the Joule heating term.

These equations are solved with the second-order Godunov-type scheme developed by T. Sano & S. Inutsuka (2004, in preparation). Operator splitting is used. The hydrodynamical part of the equations is solved by a Godunov method, using the exact solution of the simplified MHD Riemann problem. The Riemann problem is simplified by including only the tangential component of the field. The characteristic velocity is then that of the magnetosonic wave alone, and the MHD Riemann problem can be solved in a way similar to the hydrodynamical one (Colella & Woodward 1984). The piecewise linear distributions of flow quantities are calculated with a monotonicity constraint following van Leer's (1979) method. The remaining terms, the magnetic tension component of the equation of motion and the induction equation, are solved by the MoC-CT method (Stone & Norman 1992), guaranteeing $\boldsymbol{\nabla} \cdot \boldsymbol{B} = 0$ to within round-off error throughout the calculation (Evans & Hawley 1988).

The accuracy of the scheme has been demonstrated by various test problems and by calculations of the numerical growth rate of the MRI (Sano 1998; Sano & Stone 2002a). The

inclusion of the ohmic dissipation term in the CT method is straightforward. For ideal MHD, the electromotive force, $v \times B$, is defined at the edge of each cell. For resistive MHD, we evaluate the current density J at the same position and calculate a new electromotive force including the dissipation term, $-\eta J$.

The energy equation can be solved in either the total energy or the internal energy form. In most cases we use the conservative, total energy form because it allows a more complete analysis of the energy budget. In saturated turbulence driven by the MRI, the main source of heating is magnetic dissipation (Sano & Inutsuka 2001). Under nonconservative numerical schemes, magnetic energy can be lost from the system, leading to time increases in gas pressure that are slower than obtained using a total energy scheme. We use the internal energy scheme in a few models for comparing with the results of the total energy scheme.

2.2. *Initial Conditions and Normalization*

In the initial equilibrium, the tidal force in the local effective potential balances the Coriolis force, and both are much greater than magnetic forces. The relative importance of the field is given by the ratio between the gas and magnetic pressures, $\beta = P/P_{\mathrm{mag}} = (2/\gamma)c_s^2/v_A^2$, where $c_s = (\gamma P/\rho)^{1/2}$ and $v_A = B/(4\pi\rho)^{1/2}$ are the sound velocity and Alfvén speed, respectively. The initial plasma beta β_0 is larger than 100 for all the models shown in this paper. The initial distribution of the azimuthal velocity is given by $v_{y0}(x) = -q\Omega x$. The uniform density and gas pressure are assumed to be ρ_0 and P_0, respectively.

Because the evolution of the MRI is sensitive to whether the net flux of the vertical field is zero or finite, we consider two kinds of initial field geometries: a uniform vertical field $B_z = B_0$ and a field with zero net flux, $B_z(x) = B_0 \sin(2\pi x/L_x)$. Here L_x is the size of the shearing box in the radial direction.

The system of equations is normalized using the initial density ($\rho_0 = 1$) and the angular velocity ($\Omega = 10^{-3}$), following Hawley et al. (1995). However, lengths are normalized differently from previous studies so that the gas pressure dependence of the saturation level can be examined. The local shearing box has three possible scales of length: the pressure scale height $H_0 = (2/\gamma)^{1/2}c_{s0}/\Omega$, the unstable wavelength of the MRI $\lambda_0 = 2\pi v_{A0}/\Omega$, and the size of the box. Here c_{s0} and v_{A0} are the initial sound speed and Alfvén speed, respectively.

While lengths in previous work are normalized by H_0, we choose the vertical height of the box $L_z = 1$ as the unit length. Then both the gas pressure P_0 and the field strength B_0 are independent parameters and determine the ratios H_0/L_z and λ_0/L_z, respectively. Note that the ratio of the box size to the disk thickness H_0 depends on the choice of initial gas pressure P_0 in this normalization. The radial and azimuthal sizes of the shearing box are taken to be $L_x = L_z$ and $L_y = 4L_z$. The primary goal of this paper is to understand the dependence of the saturation level on physical quantities. For this purpose, we perform a few extreme models in which the box size exceeds the pressure scale height of the disk, or the gas pressure increases by 3 orders of magnitude from its initial value. Care must be taken when applying the results to real accretion disks.

Spatially uncorrelated perturbations in the gas pressure and azimuthal velocity are imposed at the beginning of each calculation. The fluctuations have a zero mean value with a maximum amplitude of $|\delta P|/P_0 = \beta_0^{-1}$ and $|\delta v|/c_{s0} = 0.1\beta_0^{-1/2}$. The amplitude of the initial fluctuations is less than 1% because $\beta_0 \geq 100$. Most of the calculations use a standard

grid resolution of $32 \times 128 \times 32$ with uniform zoning. In the azimuthal and vertical direction, periodic boundary conditions are used. For the radial boundary, a sheared periodic boundary condition (Hawley et al. 1995) is adopted.

2.3. *Heating in the Shearing Box*

In the shearing box, angular momentum is transported by Maxwell and Reynolds stresses, with sum

$$w_{xy} = -\frac{B_x B_y}{4\pi} + \rho v_x \, \delta v_y, \tag{6}$$

where $\delta v_y \equiv v_y + q\Omega x$ is the deviation from the background shear motion. The stress w_{xy} is closely related to the total energy within the box defined as

$$\Gamma \equiv \int dV \left[\rho\left(\frac{v^2}{2} + \epsilon + \phi\right) + \frac{B^2}{8\pi} \right] \tag{7}$$

(Hawley et al. 1995), where $\phi = -q\Omega^2 x^2$ is the tidal expansion of the effective potential. Using the evolution equations for the resistive MHD system (eqs. [1]–[4]), the time derivative of the above equation gives

$$
\begin{aligned}
\frac{d\Gamma}{dt} &= -\int dA \left\{ \rho v \left(\frac{v^2}{2} + \epsilon + \frac{P}{\rho} + \phi\right) \right. \\
&\quad \left. + \frac{1}{4\pi}\left[B \times (v \times B) - \eta B \times (\nabla \times B) \right] \right\} \\
&= q\Omega L_x \int_X dA \left(\rho v_x \, \delta v_y - \frac{B_x B_y}{4\pi} \right) \\
&= q\Omega L_x \int_X dA \, w_{xy},
\end{aligned} \tag{8}
$$

where dA is the surface element and the integral is taken over either of the radial boundaries. Thus, the rate of energy input through the sheared periodic radial boundary is proportional to the stress w_{xy} at the boundary. Note that the final expression of equation (8) does not explicitly depend on the resistivity.

If the stress w_{xy} at the boundary is positive or the angular momentum flux through the box is outward, the total energy of the system increases. The source of the injected energy is the background shear motion. In realistic disks, positive stresses lead to inward mass accretion, bringing a loss of gravitational energy. The gain in total energy in the shearing box represents this energy release. The injected energy goes to the magnetic field as a result of the growth of MRI. Magnetic energy is then thermalized via magnetic reconnection.

In saturated turbulence, the time-averaged magnetic and kinetic energies are nearly constant. Furthermore, the density varies little, so that the change in potential energy $\rho\phi$ is negligible compared with the other terms in equation (7). All the energy gain of the system is therefore finally deposited by the thermal energy $E_{\mathrm{th}} = P/(\gamma - 1)$, and equation (8) can be written as

$$\left\langle\left\langle \dot{E}_{\mathrm{th}} \right\rangle\right\rangle = q\Omega \left\langle\left\langle w_{xy} \right\rangle\right\rangle, \tag{9}$$

where the double brackets denote time- and volume-averaged quantities.[7] This fluctuation-dissipation relation has been clearly

---

[7] We also use the single brackets $\langle f \rangle$ to denote a volume average of quantity f.

demonstrated in numerical simulations (Sano & Inutsuka 2001). A similar relation holds in cylindrical coordinates for the global disk problem (Balbus & Papaloizou 1999).

If cooling processes are inefficient and the stress $\langle\langle w_{xy} \rangle\rangle$ is constant, the gas pressure increases linearly with time. The time evolution is approximately given by

$$\langle\langle P(t) \rangle\rangle = P_0 + q(\gamma - 1)\Omega\langle\langle w_{xy} \rangle\rangle t. \tag{10}$$

Assuming $q = 3/2$ and $\gamma = 5/3$, the plasma β would evolve as

$$\frac{\langle\langle P(t) \rangle\rangle}{\langle\langle P_{\mathrm{mag}} \rangle\rangle} = \frac{P_0}{\langle\langle P_{\mathrm{mag}} \rangle\rangle} + \Omega\frac{\langle\langle w_{xy} \rangle\rangle}{\langle\langle P_{\mathrm{mag}} \rangle\rangle} t$$

$$\approx \beta_0\frac{P_{\mathrm{mag},0}}{\langle\langle P_{\mathrm{mag}} \rangle\rangle} + 300\left(\frac{\langle\langle w_{xy} \rangle\rangle/\langle\langle P_{\mathrm{mag}} \rangle\rangle}{0.5}\right)\left(\frac{t/t_{\mathrm{rot}}}{100}\right). \tag{11}$$

Here we use a relation $\langle\langle w_{xy} \rangle\rangle/\langle\langle P_{\mathrm{mag}} \rangle\rangle \approx 0.5$ obtained in previous numerical simulations (e.g., Hawley et al. 1995). Equation (11) indicates that after 100 orbits, the plasma β must be larger than a few hundred, even though the first term on the right-hand side of equation (11) can be much smaller.

The change in gas pressure over 100 orbits can be large and should be taken into account in analyzing the effects of gas pressure.

In realistic situations, however, the gas pressure can be reduced by radiative cooling or by expansion in the vertical direction. Instead of including cooling processes, we examine the effects of cooling simply by changing the ratio of the specific heats γ. For nearly isothermal simulations, we use $\gamma = 1.001$, while $\gamma = 5/3$ is used for adiabatic simulations.

3. RESULTS

The nonlinear evolution of the MRI is investigated using three-dimensional MHD simulations. Various initial conditions are used to reveal the dependence of the saturation amplitude on physical quantities such as the gas pressure. Parameters for all the models are listed in Tables 1–3. Model names are given in column (1). The first letter in the model name denotes the initial field geometry. The labels of those with zero net vertical flux contain the letter S. Models started with a uniform B_z have a label beginning with Z. The two numbers N_1 and N_2 indicate the initial field strength and the initial plasma β, respectively. The field strength is given by $v_{A0} = B_0/(4\pi\rho_0)^{1/2} = 2^{(N_1 - 7)} \times 10^{-4}$ using the tens digit N_1,

TABLE 1
ZERO NET FLUX B_z SIMULATIONS

Model (1)	β_0 (2)	P_0 (3)	v_{A0} (4)	H_0[a] (5)	λ_0[b] (6)	Size (7)	Δ (8)	Orbits (9)	$\langle\langle w_M \rangle\rangle/P_0$ (10)	$\langle\langle w_R \rangle\rangle/P_0$ (11)	$\langle\langle P \rangle\rangle/P_0$ (12)	α[c] ($\times 10^3$) (13)
S41	10^2	7.8125×10^{-9}	1.25×10^{-5}	0.125	0.079	$1 \times 4 \times 1$	1/32	100	1.31	0.305	387	4.18
S42	10^4	7.8125×10^{-7}	1.25×10^{-5}	1.25	0.079	$1 \times 4 \times 1$	1/32	100	0.0123	0.00272	5.94	2.53
S43	10^6	7.8125×10^{-5}	1.25×10^{-5}	12.5	0.079	$1 \times 4 \times 1$	1/32	100	3.74×10^{-4}	7.02×10^{-5}	1.19	0.373
S51	10^2	3.125×10^{-8}	2.5×10^{-5}	0.25	0.16	$1 \times 4 \times 1$	1/32	300	0.611	0.121	917	0.798
S52	10^4	3.125×10^{-6}	2.5×10^{-5}	2.5	0.16	$1 \times 4 \times 1$	1/32	600	0.00799	0.00159	29.9	0.320
S53	10^6	3.125×10^{-4}	2.5×10^{-5}	25	0.16	$1 \times 4 \times 1$	1/32	300	1.21×10^{-4}	2.21×10^{-5}	1.28	0.112
S61	10^2	1.25×10^{-7}	5×10^{-5}	0.5	0.31	$1 \times 4 \times 1$	1/32	300	0.158	0.0316	259	0.731
S62	10^4	1.25×10^{-5}	5×10^{-5}	5	0.31	$1 \times 4 \times 1$	1/32	300	0.00165	3.26×10^{-4}	4.30	0.460
S63	10^6	1.25×10^{-3}	5×10^{-5}	50	0.31	$1 \times 4 \times 1$	1/32	300	4.21×10^{-5}	6.67×10^{-6}	1.10	0.0442
S71	10^2	5×10^{-7}	1.0×10^{-4}	1	0.63	$1 \times 4 \times 1$	1/32	100	0.0271	0.00569	14.4	2.27
S72	10^4	5×10^{-5}	1.0×10^{-4}	10	0.63	$1 \times 4 \times 1$	1/32	100	3.93×10^{-4}	7.89×10^{-5}	1.23	0.382
					$\gamma = 1.001$ (Isothermal)							
S51i	10^2	3.125×10^{-8}	2.5×10^{-5}	0.25	0.16	$1 \times 4 \times 1$	1/32	100	0.00135	2.71×10^{-4}	1.02	1.59
S52i	10^4	3.125×10^{-6}	2.5×10^{-5}	2.5	0.16	$1 \times 4 \times 1$	1/32	300	0.00313	7.89×10^{-4}	1.02	3.83
S53i	10^6	3.125×10^{-4}	2.5×10^{-5}	25	0.16	$1 \times 4 \times 1$	1/32	300	1.12×10^{-4}	2.08×10^{-5}	1.01	0.132
S61i	10^2	1.25×10^{-7}	5×10^{-5}	0.5	0.31	$1 \times 4 \times 1$	1/32	100	0.00856	0.00199	1.02	10.3
S62i	10^4	1.25×10^{-5}	5×10^{-5}	5	0.31	$1 \times 4 \times 1$	1/32	300	0.00111	2.31×10^{-4}	1.02	1.32
S63i	10^6	1.25×10^{-3}	5×10^{-5}	50	0.31	$1 \times 4 \times 1$	1/32	300	4.13×10^{-4}	6.94×10^{-6}	1.00	0.0480
					$\gamma = 5$							
S52g	10^4	3.125×10^{-6}	2.5×10^{-5}	2.5	0.16	$1 \times 4 \times 1$	1/32	200	0.0151	0.00257	85.6	0.206
S62g	10^4	1.25×10^{-5}	5×10^{-5}	5	0.31	$1 \times 4 \times 1$	1/32	200	0.00454	7.43×10^{-4}	28.1	0.188
				Solved by an Internal Energy (Nonconservative) Scheme								
S51e.........	10^2	3.125×10^{-8}	2.5×10^{-5}	0.25	0.16	$1 \times 4 \times 1$	1/32	300	0.321	0.0727	127	3.09
S52e.........	10^4	3.125×10^{-6}	2.5×10^{-5}	2.5	0.16	$1 \times 4 \times 1$	1/32	300	0.00475	9.61×10^{-4}	3.24	1.76
S61e.........	10^2	1.25×10^{-7}	5×10^{-5}	0.5	0.31	$1 \times 4 \times 1$	1/32	300	0.0934	0.0197	45.9	2.46
S62e.........	10^4	1.25×10^{-5}	5×10^{-5}	5	0.31	$1 \times 4 \times 1$	1/32	300	0.00143	2.92×10^{-4}	2.44	0.706

NOTES.—Time averages are taken over the last 50 orbits. For isothermal runs, time evolutions after 50 orbits are considered for the time averages.
[a] $H_0 = (2/\gamma)^{1/2}c_{s0}/\Omega = (2P_0/\rho_0)^{1/2}/\Omega$.
[b] $\lambda_0 = 2\pi v_{A0}/\Omega$.
[c] $\alpha = (\langle\langle w_R \rangle\rangle + \langle\langle w_R \rangle\rangle)/\langle\langle P \rangle\rangle$.

TABLE 2
Uniform B_z Simulations

Model (1)	β_0 (2)	P_0 (3)	v_{A0} (4)	H_0[a] (5)	λ_0[b] (6)	Size (7)	Δ (8)	Orbits (9)	$\langle\langle w_M\rangle\rangle/P_0$ (10)	$\langle\langle w_R\rangle\rangle/P_0$ (11)	$\langle\langle P\rangle\rangle/P_0$ (12)	α[c] ($\times 10^3$) (13)
Z13........	10^6	1.2207×10^{-6}	1.5625×10^{-6}	1.5625	0.0098	$1 \times 4 \times 1$	1/32	200	0.0111	0.00227	9.26	1.45
Z14........	10^8	1.2207×10^{-4}	1.5625×10^{-6}	15.625	0.0098	$1 \times 4 \times 1$	1/32	200	2.11×10^{-4}	4.04×10^{-5}	1.28	0.196
Z32........	10^4	1.9531×10^{-7}	6.25×10^{-6}	0.625	0.039	$1 \times 4 \times 1$	1/32	300	0.121	0.0241	234	0.621
Z33........	10^6	1.9531×10^{-5}	6.25×10^{-6}	6.25	0.039	$1 \times 4 \times 1$	1/32	100	0.00109	2.18×10^{-4}	1.59	0.823
Z42........	10^4	7.8125×10^{-7}	1.25×10^{-5}	1.25	0.079	$1 \times 4 \times 1$	1/32	100	0.0385	0.00758	22.4	2.06
Z43........	10^6	7.8125×10^{-5}	1.25×10^{-5}	12.5	0.079	$1 \times 4 \times 1$	1/32	100	6.67×10^{-4}	1.19×10^{-4}	1.37	0.575
Z51........	10^2	3.125×10^{-8}	2.5×10^{-5}	0.25	0.16	$1 \times 4 \times 1$	1/32	100	3.63	0.599	1.54×10^3	2.75
Z52........	10^4	3.125×10^{-6}	2.5×10^{-5}	2.5	0.16	$1 \times 4 \times 1$	1/32	100	0.0347	0.00573	17.7	2.29
Z53........	10^6	3.125×10^{-4}	2.5×10^{-5}	25	0.16	$1 \times 4 \times 1$	1/32	100	4.52×10^{-4}	6.71×10^{-5}	1.29	0.402
Z61........	10^2	1.25×10^{-7}	5×10^{-5}	0.5	0.31	$1 \times 4 \times 1$	1/32	100	2.53	0.414	1.27×10^3	2.31
Z62........	10^4	1.25×10^{-5}	5×10^{-5}	5	0.31	$1 \times 4 \times 1$	1/32	300	0.0333	0.00511	51.1	0.752
Z63........	10^6	1.25×10^{-3}	5×10^{-5}	50	0.31	$1 \times 4 \times 1$	1/32	100	4.25×10^{-4}	6.75×10^{-5}	1.23	0.399
Z72........	10^4	5×10^{-5}	1×10^{-4}	10	0.63	$1 \times 4 \times 1$	1/32	100	0.00890	0.00159	5.61	1.87
Z92........	10^4	8×10^{-4}	4×10^{-4}	40	2.5	$1 \times 4 \times 1$	1/32	50	...	...	...	...
$\gamma = 1.001$ (Isothermal)												
Z32i.......	10^4	1.9531×10^{-7}	6.25×10^{-6}	0.625	0.039	$1 \times 4 \times 1$	1/32	100	0.0361	0.00945	1.05	43.3
Z42i.......	10^4	7.8125×10^{-7}	1.25×10^{-5}	1.25	0.079	$1 \times 4 \times 1$	1/32	100	0.0294	0.00776	1.05	35.5
Z51i.......	10^2	3.125×10^{-8}	2.5×10^{-5}	0.25	0.16	$1 \times 4 \times 1$	1/32	100	0.936	0.208	1.71	668
Z52i.......	10^4	3.125×10^{-6}	2.5×10^{-5}	2.5	0.16	$1 \times 4 \times 1$	1/32	100	0.0239	0.00488	1.05	27.4
Z61i.......	10^2	1.25×10^{-7}	5×10^{-5}	0.5	0.31	$1 \times 4 \times 1$	1/32	100	1.06	0.257	1.98	667
Z62i.......	10^4	1.25×10^{-5}	5×10^{-5}	5	0.31	$1 \times 4 \times 1$	1/32	100	0.0190	0.00319	1.06	21.0
Z72i.......	10^4	5×10^{-5}	1×10^{-4}	10	0.63	$1 \times 4 \times 1$	1/32	100	0.00767	0.00141	1.04	8.68
Localized Initial Field												
Z62p......	10^4	1.25×10^{-5}	5×10^{-5}	5	0.31	$1 \times 4 \times 1$	1/32	100	0.00328	6.20×10^{-4}	2.53	1.55

Note.—Time averages are taken over the last 50 orbits.
[a] $H_0 = (2/\gamma)^{1/2} c_{s0}/\Omega = (2P_0/\rho_0)^{1/2}/\Omega$.
[b] $\lambda_0 = 2\pi v_{A0}/\Omega$.
[c] $\alpha = (\langle\langle w_M\rangle\rangle + \langle\langle w_R\rangle\rangle)/\langle\langle P\rangle\rangle$.

so that the initial field is stronger as N_1 is larger. The next digit, N_2, stands for the size of the initial plasma β ($\beta_0 = 10^{2N_2}$). Among those with the same N_1, the gas pressure is initially higher if N_2 is larger.

The suffixes indicate $\gamma = 1.001$ "isothermal" (i), $\gamma = 5$ (g), cases using the internal energy scheme (e), those started with a localized field in a small part of the disk (p), and runs with a uniform diffusivity (r) or an anomalous diffusivity (a).

Column (2) is the initial plasma beta β_0. The initial gas pressure P_0 and Alfvén speed v_{A0} are listed in columns (3) and (4), respectively. The scale height H_0 (col. [5]) and characteristic wavelength of the MRI λ_0 (col. [6] in Tables 1 and 2) are calculated from P_0 and v_{A0}. In Table 3, column (6) is the size of the magnetic diffusivity η. For all the models, we use a shearing box of size $1 \times 4 \times 1$ and a grid of $32 \times 128 \times 32$ zones. Each grid cell is a cube of size $\Delta = 1/32$. The effects of the box size and numerical resolution may be important also and are discussed in a subsequent paper.

The total evolution time in units of the rotation time is listed in column (9). In addition to model parameters, the tables include the saturation levels of a few quantities for each model. Time- and volume-averaged Maxwell and Reynolds stresses ($\langle\langle w_M\rangle\rangle$ and $\langle\langle w_R\rangle\rangle$) are listed in columns (10) and (11), respectively. The time average is taken over the last 50 orbits of each calculation and given in terms of the initial gas pressure P_0. The change in the gas pressure ($\langle\langle P\rangle\rangle/P_0$) is listed in column (12). The α parameter of Shakura & Sunyaev

(1973) is given by $\alpha = (\langle\langle w_M\rangle\rangle + \langle\langle w_R\rangle\rangle)/\langle\langle P\rangle\rangle$, which is listed in column (13). Note that normalization is done using the gas pressure in the nonlinear regime $\langle\langle P\rangle\rangle$ and not the initial value P_0.

3.1. Zero Net Flux B_z Models

3.1.1. Gas Pressure Dependence (Fiducial Models)

First, we consider the cases without net magnetic flux in the disk. The initial field is purely vertical and has a sinusoidal distribution with radius, $B_z(x) = B_0 \sin(2\pi x/L_x)$. The direction of the field is upward in $x < 0$ and downward in $x > 0$, and its average over the entire domain is zero. The typical time evolutions of (a) the magnetic energy, (b) the gas pressure, (c) the Maxwell stress, and (d) the Reynolds stress are shown in Figure 1, where time is measured in orbits $t_{rot} = 2\pi/\Omega$. The parameters of this fiducial model (S52) are $\beta_0 = 10^4$ and $P_0 = 3.125 \times 10^{-6}$. The pressure scale height and the MRI wavelength are initially $H_0 = (2/\gamma)^{1/2} c_{s0}/\Omega = 2.5$ and $\lambda_0 = 2\pi v_{A0}/\Omega = 0.16$, respectively. The calculation box size is $1 \times 4 \times 1$, so that the vertical size corresponds to $\frac{2}{5}$ of the scale height of the disk H_0.

The magnetic energy is amplified by the exponential growth of the instability during the first few orbits (see Fig. 1a). Then MHD turbulence is initiated and sustained until the end of the calculation at 600 orbits. The initial magnetic field is purely vertical, and the magnetic energy $\langle B_z^2/8\pi\rangle/P_0 \approx 5 \times 10^{-5}$.

Model (1)	β_0 (2)	P_0 (3)	v_{A0} (4)	H_0[a] (5)	η_0[b] (6)	Size (7)	Δ (8)	Orbits (9)	$\langle\langle w_M\rangle\rangle/P_0$ (10)	$\langle\langle w_R\rangle\rangle/P_0$ (11)	$\langle\langle P\rangle\rangle/P_0$ (12)	α[c] ($\times 10^3$) (13)
S51r.........	10^2	3.125×10^{-8}	2.5×10^{-5}	0.25	$10^{-7.5}$	$1\times4\times1$	1/32	300	0.521	0.104	633	0.987
S52r.........	10^4	3.125×10^{-6}	2.5×10^{-5}	2.5	$10^{-7.5}$	$1\times4\times1$	1/32	300	0.00591	0.00119	11.2	0.635
S53r.........	10^6	3.125×10^{-4}	2.5×10^{-5}	25	$10^{-7.5}$	$1\times4\times1$	1/32	150	1.27×10^{-4}	2.27×10^{-5}	1.12	0.134
S62r.........	10^4	1.25×10^{-5}	5×10^{-5}	5	$10^{-7.5}$	$1\times4\times1$	1/32	300	0.00141	2.81×10^{-4}	3.98	0.424
S51a.........	10^2	3.125×10^{-8}	2.5×10^{-5}	0.25	Anomalous	$1\times4\times1$	1/32	300	0.447	0.0905	624	0.862
S52a.........	10^4	3.125×10^{-6}	2.5×10^{-5}	2.5	Anomalous	$1\times4\times1$	1/32	300	0.00598	0.00121	8.65	0.832
S53a.........	10^6	3.125×10^{-4}	2.5×10^{-5}	25	Anomalous	$1\times4\times1$	1/32	150	9.60×10^{-5}	1.78×10^{-5}	1.09	0.105
S62a.........	10^4	1.25×10^{-5}	5×10^{-5}	5	Anomalous	$1\times4\times1$	1/32	300	0.00170	3.37×10^{-4}	4.21	0.484
Z32r.........	10^4	1.9531×10^{-7}	6.25×10^{-6}	0.625	$10^{-7.5}$	$1\times4\times1$	1/32	300	0.167	0.0321	234	0.848
Z51r.........	10^2	3.125×10^{-8}	2.5×10^{-5}	0.25	10^{-6}	$1\times4\times1$	1/32	100	1.08	0.198	529	2.42
Z52r.........	10^4	3.125×10^{-6}	2.5×10^{-5}	2.5	10^{-6}	$1\times4\times1$	1/32	100	0.0138	0.00254	7.34	2.22
Z53r.........	10^6	3.125×10^{-4}	2.5×10^{-5}	25	10^{-6}	$1\times4\times1$	1/32	100	3.01×10^{-4}	4.92×10^{-5}	1.14	0.307
Z62r.........	10^4	1.25×10^{-5}	5×10^{-5}	5	10^{-6}	$1\times4\times1$	1/32	300	0.0254	0.00428	37.7	0.788
Z32a	10^4	1.9531×10^{-7}	6.25×10^{-6}	0.625	Anomalous	$1\times4\times1$	1/32	300	0.0952	0.0187	170	0.669
Z51a	10^2	3.125×10^{-8}	2.5×10^{-5}	0.25	Anomalous	$1\times4\times1$	1/32	100	1.98	0.373	1.06×10^3	2.22
Z52a	10^4	3.125×10^{-6}	2.5×10^{-5}	2.5	Anomalous	$1\times4\times1$	1/32	100	0.0217	0.00397	13.1	1.96
Z53a	10^6	3.125×10^{-4}	2.5×10^{-5}	25	Anomalous	$1\times4\times1$	1/32	100	3.86×10^{-4}	6.51×10^{-5}	1.22	0.371
Z62a	10^4	1.25×10^{-5}	5×10^{-5}	5	Anomalous	$1\times4\times1$	1/32	300	0.0197	0.00363	34.4	0.677
				$\gamma = 1.001$ (Isothermal)								
S52ir........	10^4	3.125×10^{-6}	2.5×10^{-5}	2.5	$10^{-7.5}$	$1\times4\times1$	1/32	300	0.00230	5.98×10^{-4}	1.02	2.84
S52ia	10^4	3.125×10^{-6}	2.5×10^{-5}	2.5	Anomalous	$1\times4\times1$	1/32	300	0.00211	5.53×10^{-4}	1.02	2.62
Z52ir........	10^4	3.125×10^{-6}	2.5×10^{-5}	2.5	10^{-6}	$1\times4\times1$	1/32	100	0.0112	0.00247	1.01	13.5
Z52ia	10^4	3.125×10^{-6}	2.5×10^{-5}	2.5	Anomalous	$1\times4\times1$	1/32	100	0.0195	0.00428	1.04	22.9

NOTES.—Time averages are taken over the last 50 orbits. For isothermal runs, time evolutions after 50 orbits are considered for the time averages.

[a] $H_0 = (2/\gamma)^{1/2}c_{s0}/\Omega = (2P_0/\rho_0)^{1/2}/\Omega$.

[b] A uniform and constant diffusivity η_0 or an anomalous diffusivity is used. The anomalous diffusivity is assumed to be $\eta = k_0(v_d - v_{d0})^2$ with $k_0 = 0.05$ and $v_{d0} = 0.05$.

[c] $\alpha = (\langle\langle w_M\rangle\rangle + \langle\langle w_R\rangle\rangle)/\langle\langle P\rangle\rangle$.

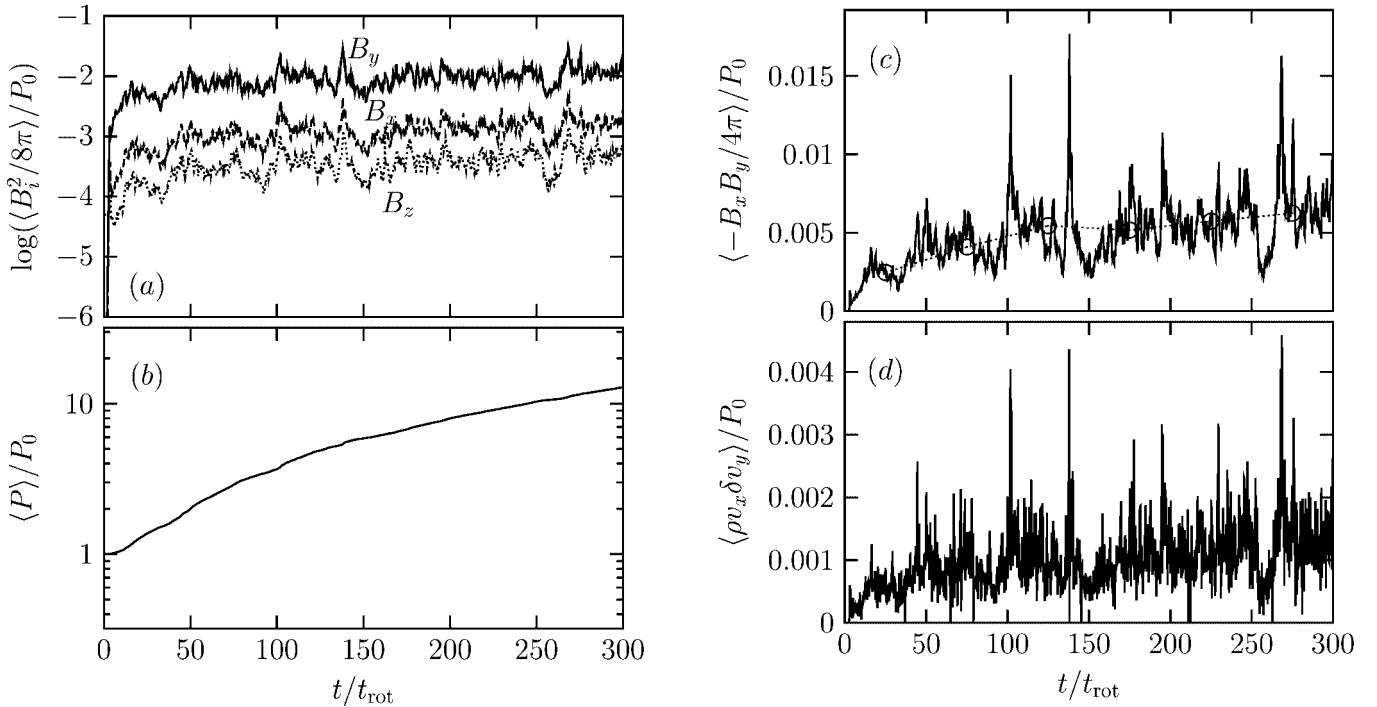FIG. 1.—Time evolution of the volume-averaged (a) magnetic energy $\langle B_i^2/8\pi\rangle/P_0$, (b) gas pressure $\langle P\rangle/P_0$, (c) Maxwell stress $\langle -B_x B_y/4\pi\rangle/P_0$, and (d) Reynolds stress $\langle \rho v_x \delta v_y\rangle/P_0$ in the fiducial model S52. The plasma β and gas pressure are initially $\beta_0 = 10^4$ and $P_0 = 3.125\times10^{-6}$, respectively. Time averages of the Maxwell stress over 50 orbit intervals are indicated by circles and show a gradual increase with time.

The saturated amplitude $\langle B^2/8\pi\rangle/P_0 \approx 5 \times 10^{-2}$ is greater by about 3 orders of magnitude. In the saturated turbulence, the azimuthal component of the magnetic pressure dominates the other components by an order of magnitude. The ratios of each component ($\langle\langle B_y^2\rangle\rangle/\langle\langle B_z^2\rangle\rangle \approx 20$ and $\langle\langle B_x^2\rangle\rangle/\langle\langle B_z^2\rangle\rangle \approx 3$) are nearly constant during the turbulent phase.

The gas pressure, on the other hand, continues to increase throughout the evolution (see Fig. 1b) because no cooling processes are included in the energy equation. The main source of heating is the dissipation of magnetic fields (Sano & Inutsuka 2001). The volume-averaged gas pressure at 300 orbits, $\langle P\rangle/P_0 \approx 12$, is much larger than the magnetic pressure in the saturated turbulent state, $\langle P_{\mathrm{mag}}\rangle/P_0 \sim 0.01$. The magnetic energy is almost saturated while the gas pressure is increasing, and thus the ratio between the magnetic and gas pressure $\beta = P/P_{\mathrm{mag}}$ increases with time throughout the calculation.

The efficiency of angular momentum transport is given by the radial-azimuthal (x-y) component of the stress tensor w_{xy}. The time evolutions of the Maxwell ($w_{\mathrm{M}} \equiv -B_x B_y/4\pi$) and Reynolds stress ($w_{\mathrm{R}} \equiv \rho v_x \,\delta v_y$) are shown in Figures 1$c$ and 1d, respectively. As is shown in previous work (e.g., Hawley et al. 1995, 1996), the Maxwell stress always dominates the Reynolds stress by a factor of about 5. The stress fluctuates with time, but the amplitude of the time variation is much smaller than in cases started with a uniform B_z (Sano & Inutsuka 2001; see § 4.1). Although the Maxwell and Reynolds stresses are nearly saturated in the nonlinear regime, the long-term evolution shows a gradual increase. To clarify this trend, we take the time average of the Maxwell stress every 50 orbits, depicted in Figure 1c by circles. A slight positive slope can be seen in the evolution of the time-averaged Maxwell stress. Hereafter, we focus on this gradual increase of the stress.

During the nonlinear turbulent phase, both the gas pressure and the Maxwell stress increase with time. Thus, it may be interesting to examine the correlation between these two quantities. In Figure 2a, the volume-averaged Maxwell stress is plotted as a function of the volume-averaged gas pressure. The models shown in this figure are S51, S52, and S53. Parameters for the three models are identical except for the initial gas pressure P_0.

Each model evolves toward the upper right on this diagram because both the gas pressure and stress increase with time. Note that the horizontal axis can be regarded as time. The increase of the gas pressure is significant when the initial value is low. For the lowest P_0 model (S51), the gas pressure at the end of the calculation is about 3 orders of magnitude larger than P_0. The evolutionary track of model S51 almost overlaps with that of S52 in the later stages. The gas pressure in the highest P_0 model (S53) is nearly constant because the initial plasma β is very large ($\beta_0 = 10^6$) for this model. The saturation level of the Maxwell stress in S53 is time independent and slightly higher than in the other two models. Figure 2a shows that higher gas pressure is associated with larger stress.

Figure 2b is the same diagram as Figure 2a, but the volume- and time-averaged values are plotted instead of the volume averages. Models S51, S52, and S53 are shown by circles, triangles, and squares, respectively. The time average is taken over every 50 orbits after 50 orbits. Obviously a power-law relation between the gas pressure and stress appears. The power-law index q of $\langle\langle w_{\mathrm{M}}\rangle\rangle \propto \langle\langle P\rangle\rangle^q$ is about $\frac{1}{4}$; that is, the Maxwell stress is roughly proportional to $P^{1/4}$.
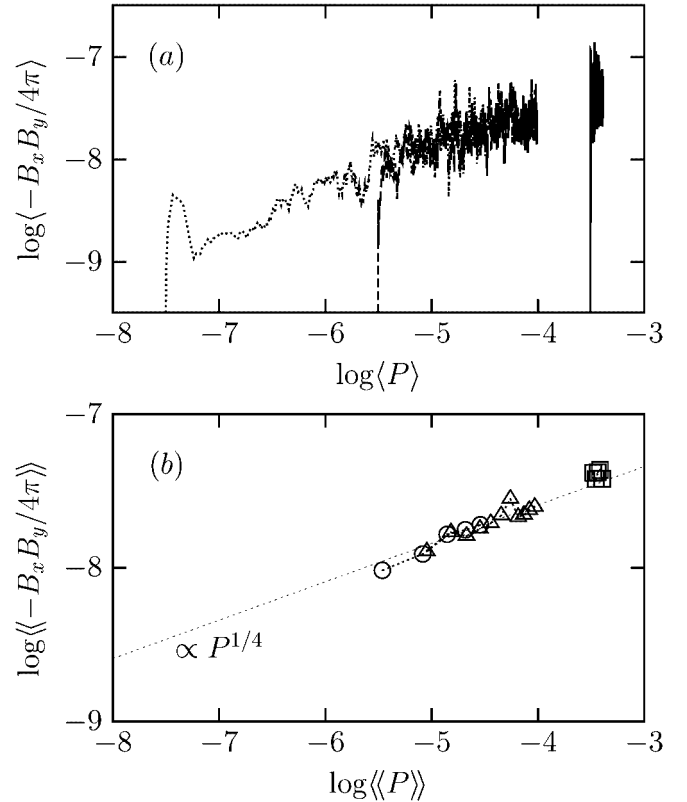

FIG. 2.—(a) Time evolution of the volume-averaged Maxwell stress $\langle -B_x B_y/4\pi\rangle$ as a function of the volume-averaged gas pressure $\langle P\rangle$ for models S51 (*dotted curve*), S52 (*dashed curve*), and S53 (*solid curve*). The parameters of these models are identical except for the initial gas pressure. (b) Time evolution of the time- and volume-averaged Maxwell stress $\langle\langle -B_x B_y/4\pi\rangle\rangle$ as a function of the time- and volume-averaged gas pressure $\langle\langle P\rangle\rangle$ for models S51 (*circles*), S52 (*triangles*), and S53 (*squares*). The time averages are taken over every 50 orbits after 50 orbits. The Maxwell stresses obtained are roughly proportional to $P^{1/4}$.

In previous work on the nonlinear development of the MRI, the initial gas pressure is usually used to normalize the stress. However, as seen from Figure 2, the gas pressure can increase by many orders of magnitude during the nonlinear evolution, and the stress depends on the gas pressure in the nonlinear regime. Thus, when analyzing long-term calculations, it may be better to normalize the stress by the gas pressure averaged over the same time interval.

The short-term variability of MRI-driven turbulence is chaotic (Winters et al. 2003). However, averaging over a longer period of 50 orbits reveals a power-law relation between $\langle\langle P\rangle\rangle$ and $\langle\langle w_{\mathrm{M}}\rangle\rangle$. To find how long an averaging period is needed, we performed two versions of calculation S52, using different spatial distributions of the initial perturbations. The time evolutions of the Maxwell stress differ. However, the stress averaged over 50 orbit periods follows the same track, shown by the dotted line in Figure 2b. Therefore, 50 orbits may be a long enough averaging period when examining the long-term evolution.

3.1.2. Independence of the Initial Field Strength

The power-law relation between the gas pressure and stress is found to be independent of the initial field strength. Figure 3 shows the saturation level of the Maxwell stress including models started with initial fields of different strengths. Models S41–S43 (*circles*) have B_0 half as strong as the fiducial ones (S51–S53), which are shown by triangles. The squares
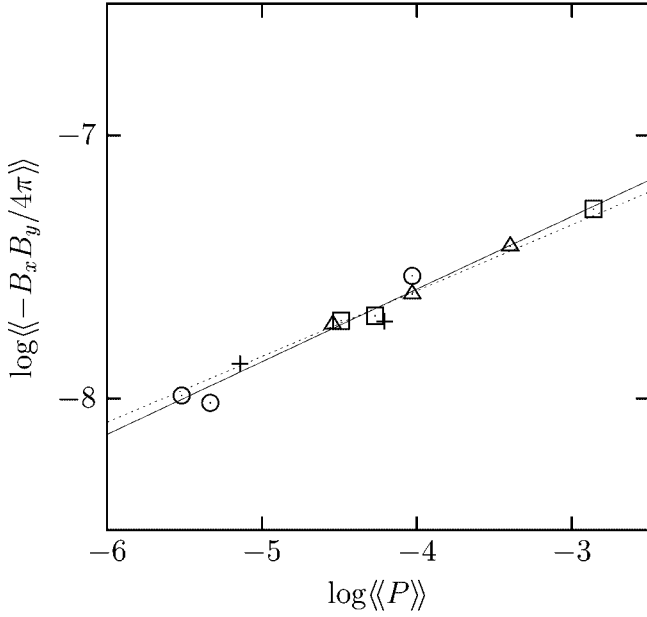
FIG. 3.—Dependence of the time-averaged Maxwell stress $\langle\langle -B_x B_y/4\pi\rangle\rangle$ on the time-averaged gas pressure $\langle\langle P\rangle\rangle$ in the nonlinear regime. Symbols indicate different initial field strengths. Circles are from models with initial Alfvén speed $v_{A0} = 1.25 \times 10^{-5}$ (S41–S43), triangles $v_{A0} = 2.5 \times 10^{-5}$ (S51–S53; fiducial), squares $v_{A0} = 5 \times 10^{-5}$ (S61–S63), and crosses $v_{A0} = 1 \times 10^{-4}$ (S71 and S72). The time average is taken over the last 50 orbits for each model. All the results are well fitted by a power-law relation $\langle\langle -B_x B_y/4\pi\rangle\rangle \propto \langle\langle P\rangle\rangle^q$. The power-law index q is about $\frac{1}{4}$ (dotted line) and the best fit is $q = 0.28$ (solid line).

(S61–S63) and crosses (S71 and S72) are those with fields 2 and 4 times stronger than the fiducial runs, respectively. The initial β value is 10^2, 10^4, or 10^6 for each B_0 case, so that the initial gas pressures differ (see Table 1). All the parameters other than B_0 and P_0 are identical for all the models shown in Figure 3. The time averages of the Maxwell stress are taken over the last 50 orbits of each calculation.

As seen from the figure, all the models follow the same evolutionary track on this diagram. The saturated stress is independent of both the initial field strength B_0 and the initial gas pressure P_0. This means that information about the initial conditions is lost in the nonlinear regime. The time-averaged stress can be fitted by a simple function of the time-averaged gas pressure in the nonlinear regime $\langle\langle P\rangle\rangle$. The power-law index is about $\frac{1}{4}$ and the best fit is $q = 0.28$ among all the models in Figure 3.

Note that if the stress is plotted against the initial gas pressure, then no clear correlation is seen. The saturation level of the stress normalized by the initial pressure widely ranges from 10^{-5} to unity (see Table 1). The gas pressure at the end of the calculation is 2–3 orders of magnitude larger than P_0 for the cases with β_0 relatively small. Thus, the choice of the normalization, P_0 or $\langle\langle P\rangle\rangle$, makes a huge difference in the normalized stress. Column (13) of Table 1 lists the total stress divided by the pressure in the nonlinear regime, $\alpha \equiv (\langle\langle w_M\rangle\rangle + \langle\langle w_R\rangle\rangle)/\langle\langle P\rangle\rangle$. The amplitude of the α parameter ranges typically from 10^{-3} to 10^{-4} with this normalization.

3.1.3. Effects of the Equation of State

In this subsection the effects of the equation of state are examined. We assume $\gamma = 5/3$ in all the models shown in Figure 3, and thus the thermal energy and gas pressure increase monotonically with time. In realistic systems, however,

cooling processes can modify the temperature of the disks. Instead of implementing cooling terms in numerical simulations, we demonstrate the effects of cooling processes simply by changing the ratio of the specific heats γ. Nearly isothermal models with $\gamma = 1.001$ are listed in Table 1. In general, the Maxwell stress in the isothermal run is smaller than that in the adiabatic run. For example, the saturation level of the Maxwell stress for model S52i is $\langle\langle w_M\rangle\rangle/P_0 = 0.0031$, which is less than half of that for the adiabatic counterpart S52. For model S52, the gas pressure at the end of the calculation is 30 times larger than P_0. The difference in the stresses may be due to an effect of the enhanced gas pressure.

The saturation levels of the Maxwell stress in models S52i, S53i, S62i, and S63i are shown in Figure 4 as a function of the gas pressure. The gas pressure in these models is unchanged throughout the calculation so that always $\langle\langle P\rangle\rangle \approx P_0$. In contrast to the adiabatic models, the time-averaged stress in the isothermal models is found to be almost constant with time. The time average is taken from 50 to 300 orbits, and the error bars in the figure show the dispersions of time averages taken every 50 orbits. The dotted line in the figure is the $\langle\langle P\rangle\rangle$-$\langle\langle w_M\rangle\rangle$ relation obtained from the adiabatic runs (Fig. 3).

The isothermal runs with the higher initial pressure P_0 have larger saturation amplitude in the stress. Furthermore, the relation between $\langle\langle w_M\rangle\rangle$ and P_0 in the isothermal runs is exactly the same as the $\langle\langle P\rangle\rangle$-$\langle\langle w_M\rangle\rangle$ relation in the adiabatic calculations. This fact indicates that the pressure-stress relation is robust and unrelated to the time-dependent behavior of the shearing box.

It is worth noticing that the horizontal axis of Figure 4 is γP. In terms of the comparison with incompressible MHD
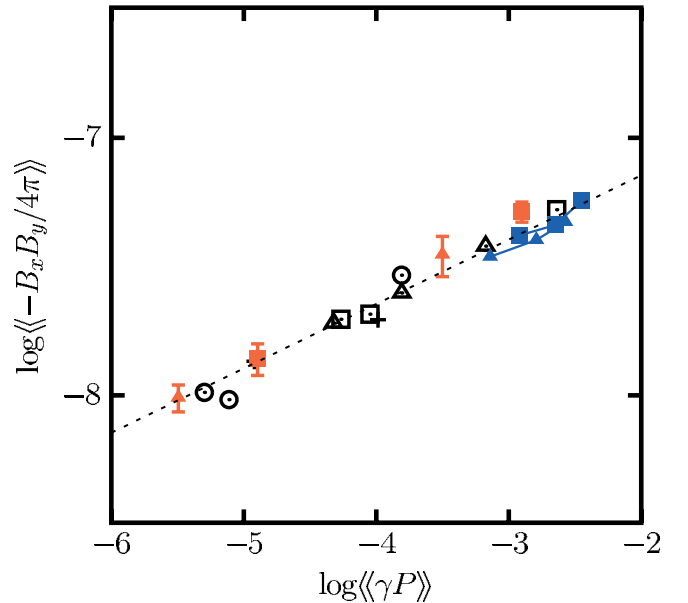

FIG. 4.—Dependence of the time-averaged Maxwell stress $\langle\langle -B_x B_y/4\pi\rangle\rangle$ on $\langle\langle\gamma P\rangle\rangle$ in the nonlinear regime. The isothermal models with $\gamma = 1.001$ are shown by red symbols; from left to right, they are models S52i, S62i, S53i, and S63i. For each model, the time average is taken from 50–300 orbits and the error bar denotes the dispersion calculated from the time averages taken every 50 orbits. Blue symbols are results of the $\gamma = 5$ models, S52g (triangles) and S62g (squares). The time average is calculated every 50 orbits after 50 orbits. The $\gamma = 5/3$ models are shown by black symbols with meanings as in Fig. 3. A dotted line shows $\langle\langle w_M\rangle\rangle \propto \langle\langle\gamma P\rangle\rangle^{1/4}$ as inferred from the models with $\gamma = 5/3$.

turbulence, the dependence on γ has an important meaning. The dependence on the gas pressure is very weak and the difference in γ between the adiabatic ($\gamma = 5/3$) and isothermal ($\gamma = 1.001$) models is quite small. Therefore, it is difficult to distinguish the dependence on P and γP. To see the difference more clearly, we consider rather extreme cases with $\gamma = 5$ (S52g and S62g), which are shown by blue symbols in the figure. Except for γ, their model parameters are identical to S52 and S62, respectively. For each model, three time averages over successive 50 orbit periods are shown. Although the range in the gas pressure is not so wide, a net increase of the saturation level with time can be seen in both models. If γP is used as the horizontal axis, the time-averaged stress in S52g and S62g is closer to the fitting function of the $\gamma = 5/3$ runs (*dotted line*). To verify the γ dependence, however, calculations with larger γ are needed. As expected from equation (10), the increase in the gas pressure is faster if γ is larger. Thus, calculations with large γ are difficult to perform using a time-explicit numerical scheme because the time step ($\propto \Delta/c_s$) becomes small. Although the saturation level of the stress may depend on γP, hereafter in this paper we use the gas pressure as the horizontal axis in similar diagrams. Direct comparison with incompressible MHD turbulence driven by the MRI may be interesting but is beyond the scope of this paper.

3.1.4. *Constraint on Numerical Resolution*

In this subsection we examine the numerical resolution needed to obtain a correct pressure-stress relation. Because the magnetic energy is proportional to the Maxwell stress in MHD turbulence, the same dependence on the gas pressure can be seen in $\langle\langle B_z^2/8\pi \rangle\rangle$. The saturation level of the vertical magnetic energy is shown in Figure 5. The dotted line indicates a fitting function obtained from all the adiabatic ($\gamma = 5/3$) models shown in Figure 3. Filled circles in Figure 5 denote the isothermal models S51i, S61i, S52i, and S62i from left to right. The saturation level of models S52i and S62i is on the dotted line. However, the lower pressure models (S51i and S62i) are located far below the predicted line. MHD turbulence in these two models decays in the late stages of the evolution, and the magnetic energy decreases with time.

Because the density is almost uniform even in the nonlinear regime, the volume-averaged magnetic energy can be regarded as the rms of the MRI wavelength,

$$\langle \lambda_{\mathrm{MRI}}^2 \rangle^{1/2} = 2\pi \frac{\langle v_{\mathrm{Az}}^2 \rangle^{1/2}}{\Omega} = \frac{2\pi}{\Omega} \left(\frac{\langle B_z^2 \rangle}{4\pi\rho_0} \right)^{1/2}. \qquad (12)$$

Throughout the paper the MRI wavelength is calculated from the vertical component of the magnetic field because the fastest growing mode of the MRI, the axisymmetric mode, is characterized by the vertical field strength. The rms of the MRI wavelength is shorter when the gas pressure is lower, if the saturation level of the magnetic energy is proportional to $P^{1/4}$. The numerical resolution in terms of the MRI wavelength is then poorer at lower gas pressures. The gap between models S61i and S52i suggests that there is a minimum resolution at which the correct $\langle\langle P \rangle\rangle$-$\langle\langle w_{\mathrm{M}} \rangle\rangle$ relation is obtained.

The horizontal dot-dashed line in Figure 5 indicates where the rms of the MRI wavelength is six grid zones. Therefore, the MRI wavelength must be resolved by at least six grid zones to avoid the decay of MHD turbulence due to numerical diffusion and to obtain the predicted saturation level. If
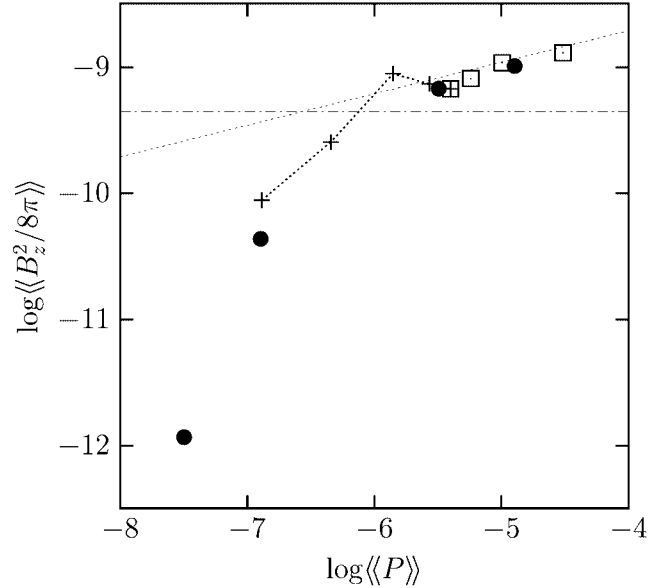

Fig. 5.—Saturation level of the vertical component of the magnetic energy $\langle\langle B_z^2/8\pi \rangle\rangle$ as a function of the gas pressure $\langle\langle P \rangle\rangle$. Models solved with $\gamma = 1.001$ (isothermal) are depicted by filled circles (from left to right, S51i, S61i, S52i, and S62i). Open squares mark results using the internal energy scheme (from left to right, S51e, S61e, S52e, and S62e). The time average is taken over the last 50 orbits for each model. Crosses show the time evolution of the time-averaged Maxwell stress in model S51e. The time averages extend over 50 orbit periods beginning at 50 orbits. A dotted line shows the predicted saturation level obtained from the models shown in Fig. 3. On the dot-dashed line, the rms of the MRI wavelength $\langle\langle \lambda_{\mathrm{MRI}}^2 \rangle\rangle^{1/2} \equiv 2\pi(\langle\langle B_z^2 \rangle\rangle/4\pi\rho_0)^{1/2}/\Omega$ is equal to six grid zones. Below this limit, saturation levels lie far below the predicted line.

$\langle\langle \lambda_{\mathrm{MRI}}^2 \rangle\rangle^{1/2} \lesssim 6\Delta$, the characteristics of the turbulence are quite different from those in well-resolved models. For example, the Reynolds stress in models S51i and S61i is larger than the Maxwell stress, while the Maxwell stress dominates the Reynolds stress in all the other models (see Table 1). This can also be seen when the ohmic dissipation is effective (Fleming, Stone, & Hawley 2000; Sano & Stone 2002b). The condition on numerical resolution may be useful not only for the local shearing box simulations but also for global disk simulations.

Figure 5 includes results obtained using a different numerical scheme. Open squares are from models S51e, S61e, S52e, and S62e, which are solved using an internal energy scheme that does not conserve total energy. The thermal energy increases more slowly as a result of energy losses from the system. For example, the gas pressure in models S52 and S52e at 300 orbits is $\langle\langle P \rangle\rangle/P_0 = 30$ and 3, respectively. However, the $\langle\langle P \rangle\rangle$-$\langle\langle w_{\mathrm{M}} \rangle\rangle$ relation is found to be unchanged, i.e., independent of the type of numerical scheme. The saturation level of the stress in the models solved by the internal energy scheme is always slightly smaller than the results of the total energy scheme (see Table 1). However, the difference can be explained clearly by the difference in gas pressure, if the power-law relation is taken into account.

Further evidence of the resolution limit can be seen in the time evolution of model S51e. Because this model is solved by the nonconservative scheme, the increase of the gas pressure is slow. Crosses in the figure mark the time averages for model S51e that are taken over every 50 orbits after 50 orbits. When the gas pressure is low and the predicted saturation level is below the resolution limit, the magnetic energy is

much lower than the dotted line. However, as the gas pressure increases and the predicted level exceeds the limit, the time-averaged magnetic energy starts to follow the predicted dotted line. This behavior indicates that we need at least about six grid zones per MRI wavelength to resolve MHD turbulence driven by the MRI.

3.2. *Uniform B_z Models*

The effects of the field geometry are examined in this section. The magnetic field structures in accretion disks are difficult to observe and remain poorly known. Therefore, it is important to survey different possible field geometries and understand the effects on the nonlinear evolution of the MRI. If the disk is penetrated by a dipole field of the central object or by a global field of the surrounding interstellar medium, there may be a net vertical flux. Here we consider models beginning with a uniform vertical field. The vertical flux is conserved in the shearing box, so that a seed field for the MRI is always present if it is present initially. Previous numerical work (Hawley et al. 1995, 1996; Sano & Stone 2002b) has shown that the existence of a net vertical flux greatly affects the nonlinear evolution of the MRI. For example, the saturation level of the stress depends on the strength of the uniform field, although the quantitative relation is not confirmed yet. The stress is reported to be proportional to B_z (Hawley et al. 1995) and to B_z^2 (Sano, Inutsuka, & Miyama 1998; Turner et al. 2003). Because the saturation amplitude may depend on several physical quantities simultaneously, it is necessary to understand all the effects in order to extract the separate contributions of the field strength and gas pressure. Therefore, we scrutinize the dependence of the saturation amplitude on the physical quantities, as well as the effects of the field geometry.

3.2.1. *Gas Pressure Dependence*

First, there is a weak power-law relation between the gas pressure and the Maxwell stress for uniform B_z models. The relation is very similar to that seen in the zero net flux models. In Figure 6 the saturation level of the Maxwell stress is shown as a function of the gas pressure. Colors denote the initial field strength, which is, from weaker to stronger, $v_{A0} = 1.5625 \times 10^{-6}$ (*black*), 6.25×10^{-6} (*cyan*), 1.25×10^{-5} (*blue*), 2.5×10^{-5} (*green*), 5×10^{-5} (*red*), and 1×10^{-4} (*pink*). The circles are from the adiabatic ($\gamma = 5/3$) models, and the squares are from the isothermal ($\gamma = 1.001$) models. Cases with the same initial field strength can be compared to extract the gas pressure dependence alone. Look at the $v_{A0} = 2.5 \times 10^{-5}$ models (*green*), for instance. The parameters of these five models are identical except for the initial gas pressure. The saturation level of the stress shows a weak dependence on P. The power-law index is about $\frac{1}{6}$ and is smaller than that in the zero net flux runs.

For purposes of comparison, the pressure-stress relation of the zero net flux models is shown by the solid line in the figure. All the results from the uniform B_z models lie above the solid line; that is, the saturation level is always higher than in the zero net flux models. A power-law relation can be seen for the other v_{A0} models as well. The power-law index is slightly smaller than, or comparable to, that of the zero net flux models.

Figure 6 includes the isothermal cases. In general, the saturation level of the stress in the isothermal models is a few times smaller than in the adiabatic counterparts. Because of
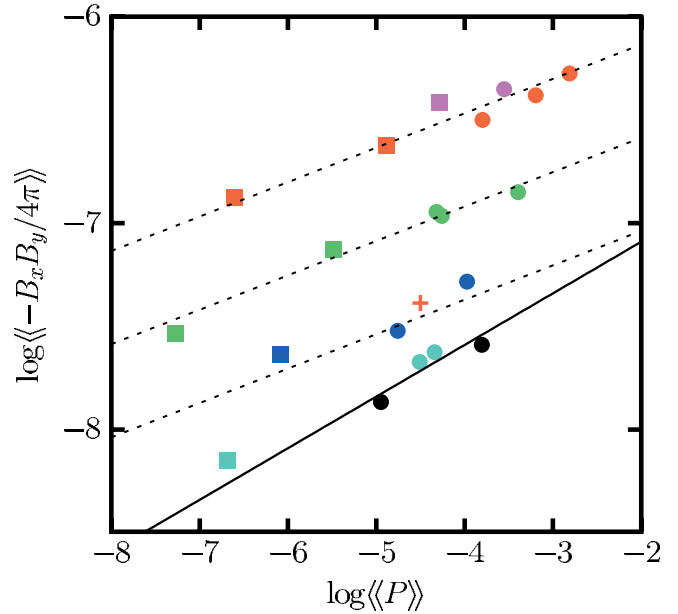

FIG. 6.—Saturation level of the Maxwell stress in the models started with uniform vertical magnetic fields. The colors of the symbols denote the strengths of the initial fields: $v_{A0} = B_0/(4\pi\rho_0)^{1/2} = 1.5625 \times 10^{-6}$ (*black*), 6.25×10^{-6} (*cyan*), 1.25×10^{-5} (*blue*), 2.5×10^{-5} (*green*), 5×10^{-5} (*red*), and 1×10^{-4} (*pink*). The adiabatic runs are shown by circles and the isothermal runs by squares. The cross is the result of model Z62p, which is started with a localized vertical magnetic field in the region $-0.25 < x < 0.25$ and $-1 < y < 1$. The total magnetic flux of this model is the same as Z42 (*blue*), while the field strength is the same as Z62 (*red*). A solid line shows the pressure-stress relation ($w_M \propto P^{1/4}$) for the zero net flux B_z models, and dotted lines are fitted functions for models Z4*, Z5*, and Z6*, with $w_M \propto P^{1/6}$.

the large stress, the increase of the gas pressure is dramatic in the adiabatic models (see eq. [10]). For model Z51, for example, the gas pressure at the end of the calculation is 3 orders of magnitude higher than the initial value. The gas pressure in the nonlinear regime is many times larger than in the isothermal model (Z51i). Therefore, the Maxwell stress with respect to $\langle\langle P \rangle\rangle$ (i.e., the α parameter) has a huge difference between the adiabatic and isothermal runs, $\alpha \approx 2.8 \times 10^{-3}$ in Z51 while $\alpha \approx 0.67$ in Z51i. For the uniform B_z cases, the α parameter ranges widely from 10^{-4} to 1 (see Table 2). The magnitude of the plasma β is approximately given by the inverse of the α parameter. The plasma β values in the nonlinear regime span a wide range, from 10 to 10^5, and there is no characteristic amplitude.

3.2.2. *Dependence on the Initial Field Strength*

As is expected, the saturation level of the stress is larger for stronger initial fields. Since the stress has a dependence on the gas pressure, as well as the field strength, both effects should be taken into account at the same time. From the results shown in Figure 6, the saturation level of the Maxwell stress is approximately given by $\langle\langle w_M \rangle\rangle \propto \langle\langle P \rangle\rangle^{1/6} v_{A0}^{3/2}$ using the gas pressure in the nonlinear regime $\langle\langle P \rangle\rangle$ and the initial field strength v_{A0}. This is plotted in the figure by dotted lines for models Z4* (*blue*), Z5* (*green*), and Z6* (*red*). Here Z4*, Z5*, and Z6* denote all the models with a uniform field of $v_{A0} = 1.25 \times 10^{-5}$, 2.5×10^{-5}, and 5×10^{-5}, respectively. For example, Z6* includes Z61, Z62, Z63, Z61i, and Z62i. The relation shown by each dotted line is valid only for one value of the initial field strength. We find that there is an upper and a lower limit to the saturation level for the uniform B_z
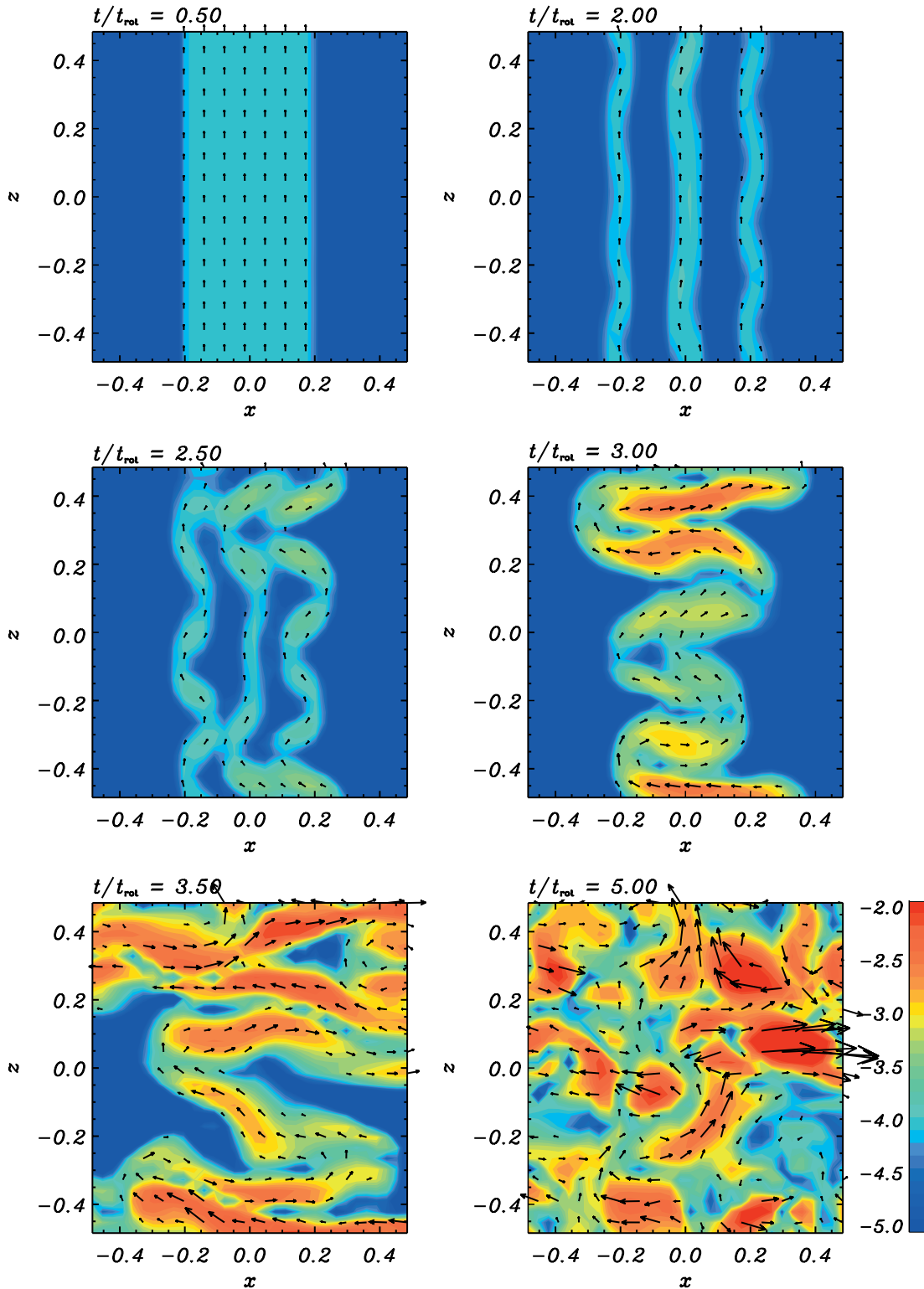
FIG. 7.—Magnetic fields in model Z62p, on x-z slices at $y = 0$. The model is started with a localized vertical field, uniform in $-0.5 < x < 0.5$ and $-1 < y < 1$. Colors show the logarithm of magnetic pressure, and arrows the strength and direction of the poloidal magnetic field. The MRI enlarges the magnetized region, and after a few orbits the entire domain is turbulent.

runs. The precise dependence on the field strength is difficult to measure because of the small range between the limits. The origins of the limits are discussed in the next subsection.

We perform an additional numerical experiment to demonstrate the importance of the amount of net magnetic flux. So far the initial field is assumed to be uniform everywhere in the computational domain. However, model Z62p has an initially uniform field that is localized within a small part of the domain. At the beginning, the magnetic field is confined to $-0.5 < x < 0.5$ and $-1 < y < 1$ and fills one-quarter of the volume of the box. The field strength and the other parameters are exactly the same as model Z62. The time evolution of the

magnetic energy density is illustrated in Figure 7 by a slice in the x-z plane at $y = 0$. The radial pattern at 2 orbits (Fig. 7, *top right panel*) is formed as a result of the background shear motion, but the field is still confined within $-0.5 < x < 0.5$. Then the magnetized region starts to spread in the radial direction as a result of the MRI. The most unstable wavelength is 0.31 in this case, so that the characteristic wavelength at 3 orbits (*middle right panel*) is consistent with the prediction of the linear analysis. When the generated horizontal field reaches nonlinear amplitude, the linear growth of the MRI is disrupted by magnetic reconnection. Through diffusion effects, the mass fraction of the magnetized region increases. Finally, at 3.5 orbits (*bottom left panel*) the whole domain is filled with amplified magnetic field and becomes turbulent. The turbulence is sustained throughout the calculation.

The saturation level of the Maxwell stress in model Z62p is indicated by the red cross in Figure 6. The initial field strength in this model is the same as in models Z6* (*red*), while the total magnetic flux is equal to that of models Z4* (*blue*). The stress in Z62p is much smaller than in models Z6* and comparable to models Z4*. Thus, the key quantity of the uniform vertical field is its total flux, or average strength over the entire system. This simple numerical experiment yields two interesting results. First, if even a small part of the disk has a magnetic field, the field can spread as a result of the shear motion of the disk and the growth of the MRI. Second, the saturation amplitude is determined by the total vertical flux.

3.2.3. *Upper and Lower Limit of the Saturation Level*

In general, saturation levels are higher for larger vertical magnetic fluxes. However, this relation has an upper and a lower limit. Figure 8 shows the time evolution of the magnetic energy for models Z32 ($v_{A0} = 6.25 \times 10^{-6}$), Z62 ($v_{A0} = 5 \times 10^{-5}$), and Z92 ($v_{A0} = 4 \times 10^{-4}$). The initial magnetic field in model Z32 is 4 times weaker than in Z62 and 16 times weaker than in Z92. The field is amplified by many orders of

FIG. 8.—Time evolution of the magnetic energy in uniform B_z models Z32 ($v_{A0} = 6.25 \times 10^{-6}$), Z62 ($v_{A0} = 5 \times 10^{-5}$), and Z92 ($v_{A0} = 4 \times 10^{-4}$). The magnetic field in model Z92 is so strong that the MRI wavelength is longer than the box size. The saturation level and time variability in model Z62 are much larger than in Z32. The large spike-shaped variations are due to the recurrent appearance and breakup of the two-channel flow.

magnitude in the lower B_0 models (Z32 and Z62). The magnetic energies in Z62 are greater than in Z32, both initially and in the nonlinear regime. On the other hand, no amplification is seen in model Z92. The reason for this behavior is explained as follows.

The shortest unstable wavelength of the MRI, or critical wavelength, is proportional to the Alfvén speed. The critical wavelength is longer for stronger initial fields. When the critical wavelength exceeds the disk scale height, linear growth of the MRI can no longer be expected. This gives the upper limit to the field strength. The critical wavelength in model Z92 is initially longer than the vertical size of the box: $\lambda_{\rm crit} = \lambda_0/\sqrt{3} \approx 1.4 > L_z$. The model is magnetorotationally stable because the magnetic tension suppresses the linear growth of the MRI. Model Z92 (*dotted line*) shows no growth in the magnetic energy.

The volume-averaged magnetic energy in model Z62 fluctuates greatly with time. The amplitude is almost an order of magnitude. The fluctuations are a typical feature of calculations with a net vertical magnetic flux. During the saturated turbulent phase, field amplification due to the growth of a channel solution occurs quasi-periodically and is followed by dissipation through magnetic reconnection (Sano & Inutsuka 2001). In weaker B_0 models, on the other hand, the two-channel flow appears less often, and the time variations are of smaller amplitudes. If the net vertical flux is less than a critical value, the saturation level of the stress approaches that of the zero net flux results.

In Figure 6 the pressure-stress relation obtained from the zero net flux runs is shown by a solid line. The field strength in models Z3* (*cyan*) is half that in models Z4* (*blue*). The field in models Z1* (*black*) is 8 times weaker than in models Z4*. However, the differences in the stress are small, and the weaker field results are almost on the solid line. This fact suggests that the saturation amplitude of the zero net flux runs gives the minimum level. The recurrent growth of the channel flow enhances the saturation level of the stress when the disk has a vertical flux. The enhancement is seen only when the field strength is large enough that the initial MRI wavelength λ_0 corresponds to at least several percent of the system size.

The two-channel flow appears if the vertical field is amplified such that the MRI wavelength corresponds to the vertical box size. The vertical field must be amplified by a larger factor to produce the channel flow if the initial field is weaker. Thus, the appearance of the two-channel flow is rarer in the weaker initial field models. Within the region of parameter space we explored, the zero net flux models and the weak uniform field models show the same level of saturation in the Maxwell stress. For those models, the power-law index in the pressure-stress relation is about $\frac{1}{4}$.

If the MRI wavelength of the initial uniform field is longer than about one-tenth of the vertical box size, the appearance of the two-channel flow enhances the saturation level of the stress. In this parameter regime, the saturation amplitude is roughly proportional to $B_0^{3/2}$, and the power-law index is slightly smaller ($\sim\frac{1}{6}$). The upper limit on the saturation level is given by a condition that the MRI wavelength corresponding to the uniform vertical field should be smaller than the vertical domain size.

Even in cases with the most unstable wavelength initially less than the grid size (e.g., model Z13), the longer wavelength unstable modes can be resolved. Furthermore, the characteristic wavelength in the nonlinear stage is longer because of the amplification of the field. Thus, the resolution
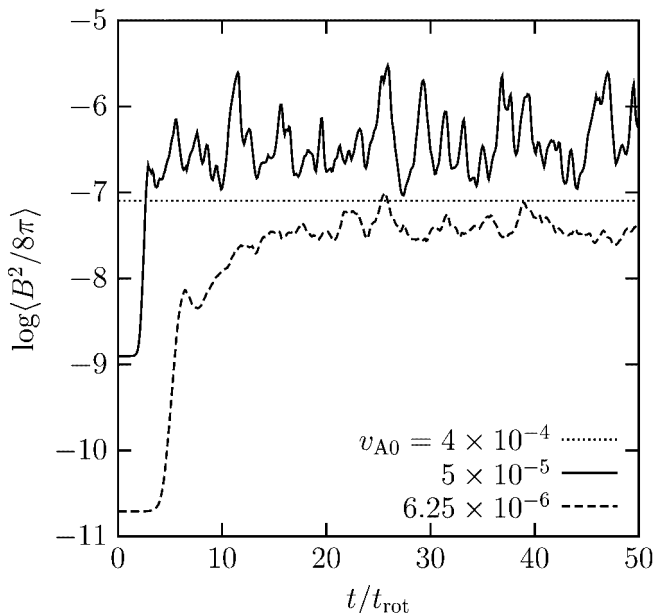
condition discussed in § 3.1.4 is satisfied in the saturated state in all the models shown in Figure 6.

3.3. *Effects of Magnetic Dissipation*

Dissipation of the magnetic field may play an important role in determining the saturation level of the MRI because magnetic reconnection occurs frequently during the saturated turbulent phase. The ideal MHD approximation is made in all the calculations listed in Tables 1 and 2. As a result of numerical diffusion, magnetic reconnection occurs even in the ideal MHD simulations. In this section we briefly examine the effects of physical dissipation. The ohmic dissipation term is explicitly included when solving the induction equation. Two types of resistivity are considered: a time-constant and spatially uniform value $\eta = \eta_0$, and an anomalous resistivity. The anomalous diffusivity adopted varies as $\eta = k_0(v_d - v_{d0})^2$ for $v_d > v_{d0}$ and $\eta = 0$ for $v_d < v_{d0}$, where $v_d \equiv |\boldsymbol{J}|/\rho$ is the drift velocity and k_0 and v_{d0} are parameters. This prescription is based on the idea that current-driven instabilities enhance the effective diffusivity and has been used in many astrophysical simulations (e.g., Yokoyama & Shibata 1994; Machida & Matsumoto 2003).

Table 3 lists the resistive models, including both those with zero net flux and those with uniform vertical initial fields. The size of the ohmic dissipation is indicated by the magnetic Reynolds number $\mathrm{Re}_M = VL/\eta$, where V and L are typical velocity and length scales, respectively. For the MRI, typical scales are the Alfvén speed $V \sim v_A$ and the most unstable wavelength $L \sim v_A/\Omega$. The magnetic Reynolds number is then $\mathrm{Re}_M = v_A^2/\eta\Omega$. Linear and nonlinear evolution of the MRI is characterized very well using the parameter Re_M (Sano & Miyama 1999; Sano & Stone 2002b).

Dissipation effects are better resolved for larger η. However, ohmic dissipation suppresses the MRI if the diffusivity is too large. The critical value of the initial magnetic Reynolds number is about 10 for zero net flux cases (Sano & Stone 2002b). Actually, MHD turbulence dies away in 100 orbits when a uniform diffusivity is added to models S51 and S52 with $\eta_0 = 10^{-7}$, corresponding to $\mathrm{Re}_M = 6.3$. Therefore, we choose $\eta_0 = 10^{-7.5}$ ($\mathrm{Re}_M = 20$) for the uniform diffusivity in zero net flux models. For uniform B_z cases, on the other hand, the critical Re_M is about unity (Sano & Stone 2002b). Thus, the diffusivity for models Z51r, Z52r, Z53r, and Z52ir is assumed to be 10^{-6}, corresponding to $\mathrm{Re}_M = 0.63$. For cases with anomalous diffusivity, we take $k_0 = 0.05$ and $v_{d0} = 0.05$ because the mean value of η in the nonlinear regime in regions with $v_d > v_{d0}$ is then a few times 10^{-8} in the zero net flux models and a few times 10^{-7} in the uniform B_z models.

The pressure-stress relations in the resistive runs are shown in Figures 9a (zero net flux B_z) and 9b (uniform B_z) together with the ideal MHD results (*circles*). Models S51, S52, S53, and S52i are shown in Figure 9a and models Z51, Z52, Z53, and Z52i are in Figure 9b. Model parameters in the resistive runs are identical to these ideal MHD models except for the magnetic diffusivity. A positive correlation can be seen for both the uniform (*squares*) and anomalous diffusivity runs (*crosses*). The saturation amplitude in the resistive runs is slightly lower than that in the $\eta = 0$ cases. However, the difference is at most a factor of 3 because the dependence on the diffusivity is weak when the magnetic Reynolds number is larger than unity (Sano & Stone 2002b). The dotted lines in the figure indicate the power-law relation $\langle\langle w_M \rangle\rangle \propto \langle\langle P \rangle\rangle^q$ with $q = \frac{1}{4}$ (Fig. 9a) and $q = \frac{1}{6}$ (Fig. 9b). The values of the
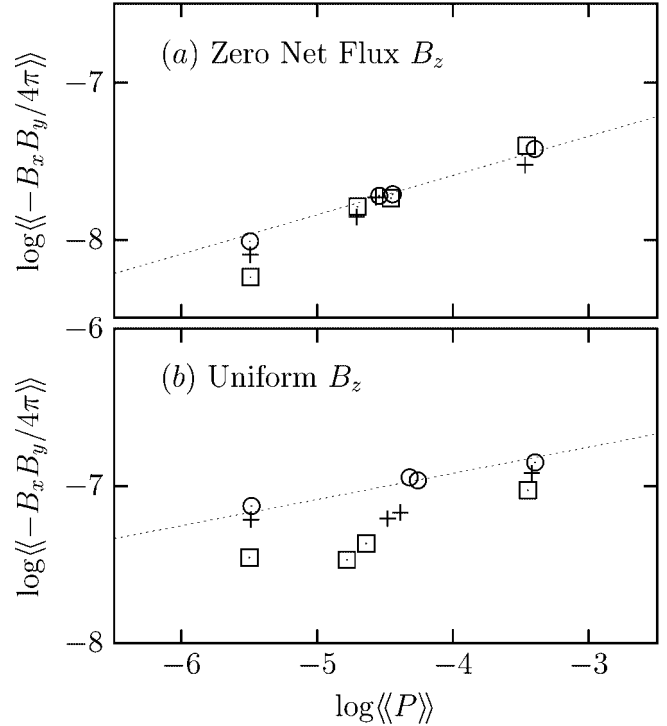

Fig. 9.—Saturation levels of the Maxwell stress in (*a*) zero net flux B_z models (S51, S52, S53, and S52i) and (*b*) uniform B_z models (Z51, Z52, Z53, and Z52i). Circles are from the ideal MHD cases. Squares are from resistive cases with uniform magnetic diffusivity $\eta = \eta_0$, and crosses are from cases with an anomalous diffusivity $\eta = k_0(v_d - v_{d0})^2$, where v_d is the drift velocity. Dotted lines indicate power laws with exponents (*a*) $q = \frac{1}{4}$ and (*b*) $q = \frac{1}{6}$.

index q for the resistive runs are similar to those in the ideal MHD runs.

The diffusion length for the magnetic field is roughly $l_{\mathrm{diff}} = 2\pi\eta/v_{Az}$. In the uniform B_z models, this scale is well resolved initially because $l_{\mathrm{diff}} = 2\pi\eta/v_{A0} \approx 8\Delta$. In the nonlinear regime, the average diffusion length is still larger than the grid scale ($\langle l_{\mathrm{diff}} \rangle = 2\pi\eta/\langle v_{Az}^2 \rangle^{1/2} \sim 3\Delta$). However, because of the severe constraint on the initial Re_M, the diffusion length in the zero net flux models is shorter than the grid scale ($\langle l_{\mathrm{diff}} \rangle/\Delta \approx 0.4$). We therefore carried out double-resolution versions of the calculations shown in Figure 9a, using $64 \times 256 \times 64$ zones. The dependence on the gas pressure is qualitatively unaffected by the change in the numerical resolution. We conclude that the weak power-law relation between the gas pressure and the Maxwell stress exists for both the ideal and resistive MHD cases.

3.4. *General Features of the Turbulence*

3.4.1. *Characteristic Quantities*

The numerical calculations discussed above show that the saturation level depends on the gas pressure, the field strength and geometry, and the equation of state. At the same time, the saturated states in all these calculations show common features.

Table 4 lists characteristic quantities in turbulence driven by the MRI. The quantities are averages from all the models listed in Tables 1–3, excepting poorly resolved cases (S51i and S61i) and a stable model (Z92). The averages include even the isothermal models, the $\gamma = 5$ models, and the resistive models. The ratios listed are independent of the initial

TABLE 4
CHARACTERISTIC RATIOS IN MRI TURBULENCE

Quantity	Average
$\langle\langle -B_x B_y/4\pi\rangle\rangle/\langle\langle B^2/8\pi\rangle\rangle$	0.467 ± 0.040
$\langle\langle -B_x B_y/4\pi\rangle\rangle/\langle\langle \rho v_x \delta v_y\rangle\rangle$	5.19 ± 0.67
$\langle\langle B_x^2\rangle\rangle/\langle\langle B_z^2\rangle\rangle$	3.35 ± 0.28
$\langle\langle B_y^2\rangle\rangle/\langle\langle B_z^2\rangle\rangle$	23.7 ± 4.0
$\langle\langle v_x^2\rangle\rangle/\langle\langle v_z^2\rangle\rangle$	2.62 ± 0.48
$\langle\langle \delta v_y^2\rangle\rangle/\langle\langle v_z^2\rangle\rangle$	2.15 ± 0.34
$\langle\langle \delta E_{\rm kin}\rangle\rangle/\langle\langle E_{\rm mag}\rangle\rangle$	0.326 ± 0.036

conditions and field configuration. The standard deviations among the models are included in the table after $\pm$.

The most interesting ratio in Table 4 is that of the Maxwell stress to the magnetic pressure. The ratio is about $\langle\langle w_{\rm M}\rangle\rangle/\langle\langle P_{\rm mag}\rangle\rangle = 0.46$ and takes a similar value for all the models. Because the Maxwell stress is always about 5 times the Reynolds stress, the total stress is approximately proportional to the magnetic pressure in the MRI turbulence. The shear motion preferentially enhances the toroidal field, so that B_y is always the dominant component. The pressures in the components of the field have universal ratios, $\langle\langle B_y^2\rangle\rangle/\langle\langle B_z^2\rangle\rangle = 23$ and $\langle\langle B_x^2\rangle\rangle/\langle\langle B_z^2\rangle\rangle = 3.3$. The magnetic field in the turbulence is anisotropic. On the other hand, anisotropy in the perturbed velocity is rather weak, with $\langle\langle \delta v_y^2\rangle\rangle/\langle\langle v_z^2\rangle\rangle = 2.2$ and $\langle\langle v_x^2\rangle\rangle/\langle\langle v_z^2\rangle\rangle = 2.6$. The ratios listed in Table 4 are valid for well-developed turbulence driven by the MRI. If ohmic dissipation is effective and MRI is suppressed, then the ratios take quite different values (Sano & Stone 2002b).

The magnetic energy density in MRI-driven turbulence is correlated with the perturbed kinetic energy $\delta E_{\rm kin} \equiv \rho\, \delta v^2/2$, and not with the total kinetic energy. The ratio is typically $\langle\langle \delta E_{\rm kin}\rangle\rangle/\langle\langle E_{\rm mag}\rangle\rangle = 0.33$. On the other hand, the ratio of thermal to magnetic energy has no universal value and ranges from 10 to 10^6 in our models. As seen from the pressure-stress relation, the ratio of magnetic to thermal energy varies approximately as $E_{\rm mag}/E_{\rm th} \propto P^{-3/4}$ for zero net flux runs. Thus, this ratio depends on the gas pressure in the nonlinear regime. This appears to be inconsistent with results of global disk simulations, in which typically $\beta \sim 100$ (e.g., Igumenshchev, Narayan, & Abramowicz 2003). The difference may be due partly to the local approximation. In the shearing box simulations, the box height is assumed fixed, while in the global simulations, the thickness of the disk can change with the pressure. For a complete comparison with the global simulations, a quantitative understanding of the effects of both box size and gas pressure is required. Box size effects will be discussed in a subsequent paper.

3.4.2. Fluctuations

MHD turbulence in our simulations is driven by the MRI. Fluctuations begin mainly by the growth of unstable modes of the MRI and initially take the form of perturbations in the magnetic field and velocity. The fluctuations in magnetic pressure may affect the distribution of the gas pressure. We find that the amplitudes of the fluctuations in the magnetic and gas pressures are always comparable in the turbulent regime. The spatial dispersion of the pressure, $\langle \delta P^2\rangle^{1/2} \equiv \langle (P - \langle P\rangle)^2\rangle^{1/2}$, is evaluated from a snapshot of the spatial distribution of the pressure. Figure 10 shows the dispersions of both the magnetic and gas pressure for all the models listed in Tables 1–3. Here the poor resolution models (S51i and S61i) and stable model

(Z92) are excluded. For each model, a snapshot is chosen from near the end of the calculation. The time variation in the saturation level is quite large for the uniform B_z runs because two phases occur. In one phase, a two-channel flow dominates, and in the other, the field is weaker and the turbulence is disorganized. For some of the uniform B_z models (Z51, Z61, Z51i, Z52i, Z61i, and Z62i), the spatial dispersions of 10 randomly selected snapshots from the saturated turbulence are plotted in the figure, so as to include information about both of the phases. Open and filled symbols are from the isothermal and adiabatic runs, respectively. Circles denote zero net flux B_z runs, and squares are from the uniform B_z runs. Evidently the relation $\langle \delta P^2\rangle^{1/2} \approx \langle P_{\rm mag}^2\rangle^{1/2}$ holds for all the models shown in this figure.

Figure 11 shows the spatial dispersions of the density (circles) and magnetic pressure (squares) as functions of the ratio of volume-averaged magnetic pressure to volume-averaged gas pressure, $\langle P_{\rm mag}\rangle/\langle P\rangle$. Again, open symbols are from isothermal models, and filled symbols are from adiabatic models. The gas pressure in the adiabatic models increases significantly in the nonlinear regime, so that gas pressure is much greater than magnetic pressure. The ratio $\langle P_{\rm mag}\rangle/\langle P\rangle$ in the adiabatic models (filled symbols) is always less than 0.01. In the isothermal models, on the other hand, the magnetic pressure can be comparable to the gas pressure.

For both the adiabatic and isothermal cases, the fluctuation in $\langle P_{\rm mag}\rangle$ is independent of $\langle P_{\rm mag}\rangle/\langle P\rangle$ and near unity, if the magnetic pressure is lower than the gas pressure. If $\langle P_{\rm mag}\rangle \sim \langle P\rangle$, then the fluctuation is slightly less. Taking account of the compressibility, the linear growth rate of the axisymmetric MRI is reduced when the toroidal component of the magnetic pressure is comparable to the gas pressure (Blaes & Balbus 1994; Kim & Ostriker 2000). This may reduce the fluctuations in the magnetic field. The density fluctuation, on the other
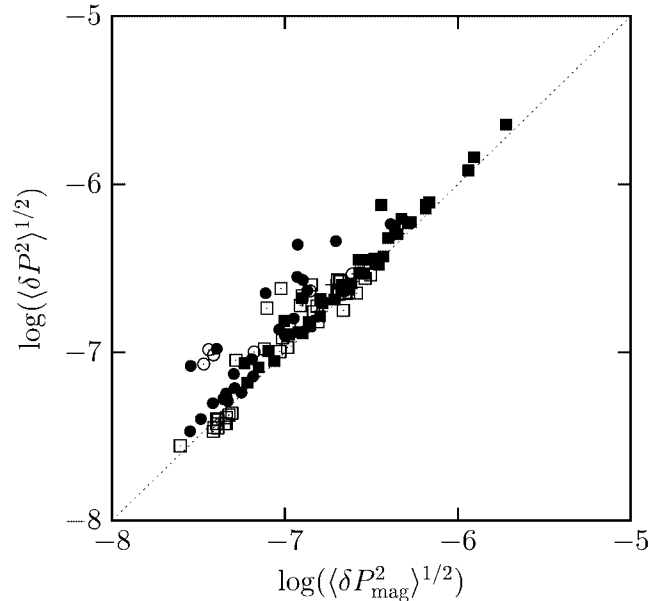

FIG. 10.—Sizes of fluctuations in the gas and magnetic pressures in the turbulent regime. All the models listed in Tables 1–3 are included except for S51i and S61i (poor resolution) and Z92 (magnetorotationally stable). For several models (Z51, Z61, Z51i, Z52i, Z61i, and Z62i), the dispersions of 10 randomly selected snapshots are also plotted. Open and filled symbols are from isothermal and adiabatic runs, respectively. Circles denote the zero net flux B_z runs, and squares are from the uniform B_z runs. Crosses indicate 10 snapshots from model Z62i.
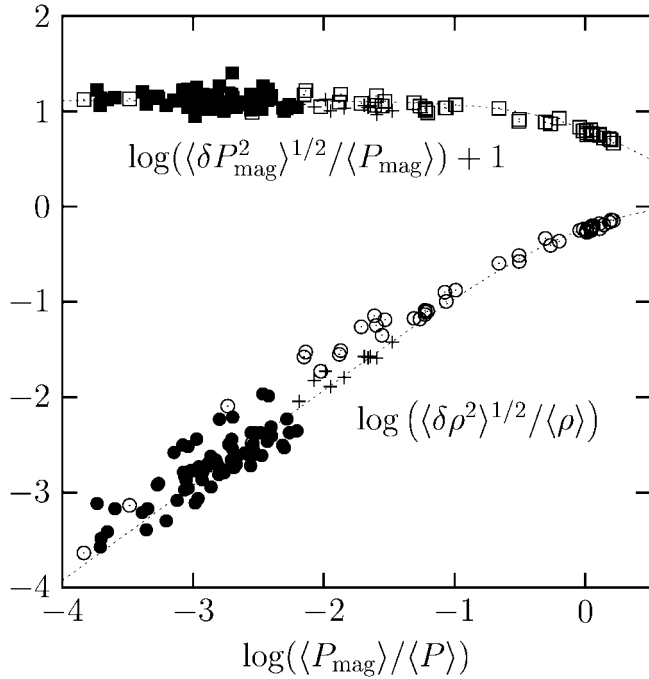
Fig. 11.—Sizes of fluctuations in the density (*circles*) and the magnetic pressure (*squares*) as functions of the ratio of magnetic to gas pressure. Open and filled symbols are from isothermal and adiabatic runs, respectively. Crosses are from 10 snapshots of model Z62i. The same models are plotted as in Fig. 10. All the data are well fitted by functions $\langle \delta P_{\mathrm{mag}}^2 \rangle^{1/2} / \langle P_{\mathrm{mag}} \rangle \approx \left(\langle P_{\mathrm{mag}} \rangle / \langle P \rangle + 1 \right)^{-1}$ and $\langle \delta \rho^2 \rangle^{1/2} / \langle \rho \rangle \approx \left(\langle P \rangle / \langle P_{\mathrm{mag}} \rangle + 1 \right)^{-1}$.

hand, is proportional to the ratio of magnetic to gas pressure. In the adiabatic cases the density is almost spatially uniform (*filled symbols*) because the magnetic pressure is much less than the gas pressure in the saturated state. Only when $\langle P_{\mathrm{mag}} \rangle$ is comparable to $\langle P \rangle$ do order unity density fluctuations occur.

All the data plotted in Figure 11 are well fitted by functions $\langle \delta P_{\mathrm{mag}}^2 \rangle^{1/2} / \langle P_{\mathrm{mag}} \rangle \approx \left(\langle P_{\mathrm{mag}} \rangle / \langle P \rangle + 1 \right)^{-1}$ and $\langle \delta \rho^2 \rangle^{1/2} / \langle \rho \rangle \approx \left(\langle P \rangle / \langle P_{\mathrm{mag}} \rangle + 1 \right)^{-1}$, which are shown by dotted curves. Crosses in the figure are obtained from 10 snapshots of model Z62i. Although the density fluctuation and magnetic pressure are time dependent, the variations move the model along the same relations in this diagram. The amplitude of density fluctuations in MRI turbulence is found to be given by

$$\frac{\langle \delta \rho^2 \rangle^{1/2}}{\langle \rho \rangle} \approx \frac{\langle \delta P_{\mathrm{mag}}^2 \rangle^{1/2}}{\langle P \rangle}. \tag{13}$$

This relation is valid for all the models we performed. Large density fluctuations are found only when the fluctuations in magnetic pressure are comparable to the gas pressure.

Where radiation pressure is important, the relationship between the fluctuations is more complicated. In radiation-dominated disks, the presence of large density fluctuations in MRI turbulence requires fast radiative diffusion, as well as magnetic pressures comparable to the gas pressure (Turner, Stone, & Sano 2002; Turner et al. 2003). In such disks, the role of the gas pressure is sometimes played by gas and radiation pressures together, depending on the radiative diffusion time-scale. When the diffusion length and MRI wavelength are comparable, the effective pressure is intermediate between the gas and total pressures. Equation (13) may hold in radiation-dominated disks if the gas pressure is replaced by the effective

pressure. The equation might be used to estimate the effective pressure from the fluctuations.

The energy density of the fluctuations in MHD turbulence is an interesting quantity in terms of the energy balance. Equipartition is found to hold between the kinetic and magnetic energies of fluctuations (Fig. 12). The symbols in the figure are the same as in Figure 10. Here the perturbed magnetic energy is defined as $\langle \delta B^2 / 8\pi \rangle \equiv \langle (|B| - \langle |B| \rangle)^2 / 8\pi \rangle$. The disturbances in kinetic and magnetic energies shown in Figure 12 both originate from unstable modes of the MRI, and the two are roughly equal throughout the saturated turbulence. The thermal energy of the perturbations, on the other hand, is not in equipartition and is comparable to or less than the magnetic energy. Figure 13 shows the thermal energy of the disturbances as a function of the magnetic energy. The size of the thermal disturbances is estimated using the internal energy of sound waves $\langle c_s^2 \delta \rho^2 / 2\rho \rangle$ (e.g., Landau & Lifshitz 1959). The gas pressure increases with time in the adiabatic shearing box calculations, and the ratio $\langle P_{\mathrm{mag}} \rangle / \langle P \rangle$ decreases. The density fluctuation is proportional to this ratio, so that $\langle \delta \rho^2 \rangle$ also decreases with time. Therefore, the thermal energy of perturbations cannot reach an equilibrium state, while the magnetic and kinetic energies are in equipartition and almost saturated.

4. DISCUSSION

4.1. *Time Variability*

The stresses generated by the MRI fluctuate greatly over time. Since the stresses control the loss of gravitational energy from accreting material, the radiation emitted locally by the disk may also vary. Here we focus on the characteristics of the time variability of the stress in our numerical simulations.

4.1.1. *Amplitude of Time Variation*

Time variability is shown in Figure 14. The temporal dispersion of the stress during the last 50 orbits of each calculation is normalized by the time-averaged stress and plotted as a function of the mean vertical component of the magnetic energy over the same interval. The zero net flux runs listed in
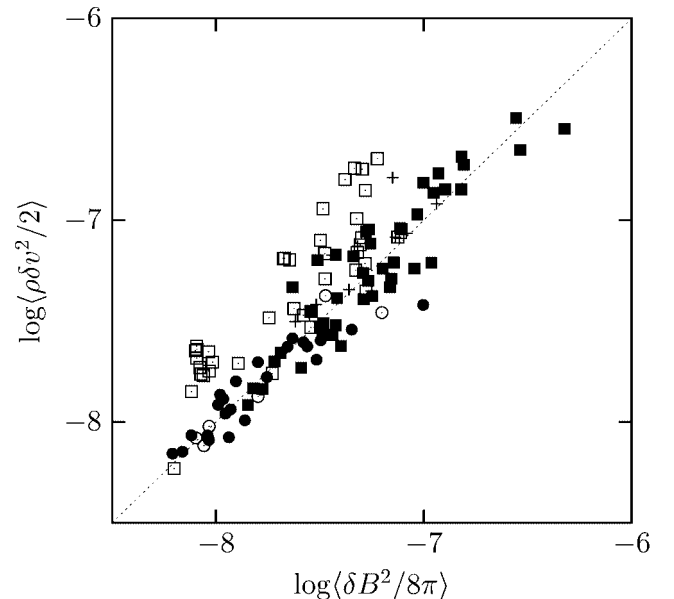

Fig. 12.—Kinetic and magnetic energies of fluctuations. The models plotted and the meanings of the symbols are identical to those in Fig. 10. A dotted line marks equipartition, $x = y$.
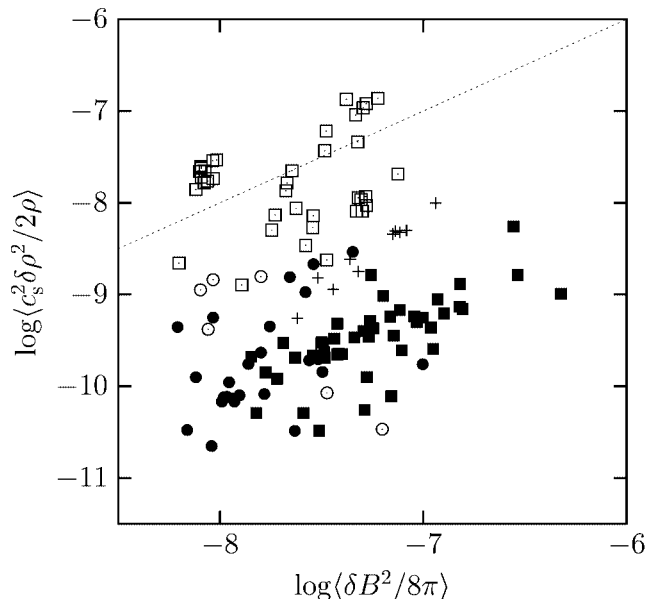
FIG. 13.—Thermal and magnetic energies of fluctuations. The models plotted and the meanings of the symbols are identical to those in Fig. 10. A dotted line marks equipartition, $x = y$.

4.1.2. Temporal Power Spectra

The power spectrum is a tool used to make comparisons with observations. Power spectral density (PSD) can be calculated from the history of the volume-averaged stress. Kawaguchi et al. (2000) found in global disk MHD simulations that the PSD of the stress has a shape similar to the PSD of the X-ray flux in observations of black hole candidates.

Figure 15 shows the PSD for three models Z62r (strong uniform field), Z32r (weak uniform field), and S62r (zero net flux). They are calculated from the history of the Maxwell stress measured at intervals $10^{-3} t_{\rm rot}$. The normalized PSDs shown in Figure 15 are obtained by the following procedure. The history data from 50 to 300 orbits are divided into eight intervals of about 30 orbits each. The PSD is calculated for each segment and the amplitude is normalized by the squared time average of the stress of each term. Then the PSD averaged over these eight spectra is shown in the figure. The error bars are standard errors $\sigma / N^{1/2}$ of the eight segments. Note that the bottom two models in the figure are shifted downward to avoid overlapping; the amplitude of the spectrum is multiplied by 10^{-2} and 10^{-4} for model Z32r and S62r, respectively.

A uniform diffusivity $\eta_0 = 10^{-6}$ is used in model Z62r. The diffusion length is $l_{\rm diff}/\Delta \approx 4$, and the effects of ohmic dissipation can be adequately resolved. MRI turbulence is prevented by diffusion if the magnetic Reynolds number, defined using the MRI wavelength and the Alfvén speed, is less than unity (Sano & Stone 2002b). In model Z32r, a diffusivity $\eta_0 = 10^{-6}$ corresponds to magnetic Reynolds number 0.039. For sustained turbulence in model Z32r, we therefore use a lower diffusivity $\eta_0 = 10^{-7.5}$, corresponding to $\mathrm{Re}_M = 1.2$ and $l_{\rm diff}/\Delta \approx 1$.

Table 1 are marked by open circles. The amplitudes in these models are typically 0.2–0.4, and the average of 0.34 is shown by a horizontal solid line. The uniform B_z models are plotted by colored symbols, with meanings as in Figure 6. When the magnetic energy in the uniform B_z models is relatively low, the time variations are comparable to those in the zero net flux models. However, time variations are larger in models with higher magnetic energies.

The large variations in the uniform vertical field cases result from recurrent growth of the two-channel flow. This flow arises from a linearly unstable MRI mode and is an exact solution of the full nonlinear MHD equations in the incompressible limit (Goodman & Xu 1994). The flows grow to nonlinear amplitudes before being disrupted by shear instabilities and magnetic reconnection. Two-channel flows occur when the MRI wavelength is comparable to the vertical height of the shearing box. The time variability is sensitive to the ratio of the MRI wavelength $\lambda_{\rm MRI}$ to the vertical box size L_z. The vertical dotted line in the figure indicates where the rms of the MRI wavelength, $\langle\langle \lambda_{\rm MRI}^2 \rangle\rangle^{1/2} = 2\pi \langle\langle v_{\rm Az}^2 \rangle\rangle^{1/2}/\Omega$, equals the box height. Time variations of order unity occur in models with $\langle\langle \lambda_{\rm MRI}^2 \rangle\rangle^{1/2} \sim L_z$. When the MRI wavelength is shorter, the growth of unstable modes and the dissipation by reconnection occur in multiple small regions simultaneously, and the overall time variations are smoother. The characteristics of the time variation illustrated in Figure 14 are little changed by the inclusion of magnetic diffusivity and by increases in numerical resolution up to $128 \times 512 \times 128$.

The observed amplitudes of X-ray variability in black hole candidates and active galactic nuclei are typically about 0.3 (e.g., Nowak et al. 1999; Papadakis et al. 2002). Local stress variations of similar size may occur if the MRI wavelength is an order of magnitude shorter than the disk thickness. However, radiative processes must be taken into account for more detailed comparison with the observations. Moreover, the amplitude may be sensitive to global effects, as it depends on the size of the box. It may be interesting to compare observed variability with results from future global disk simulations.
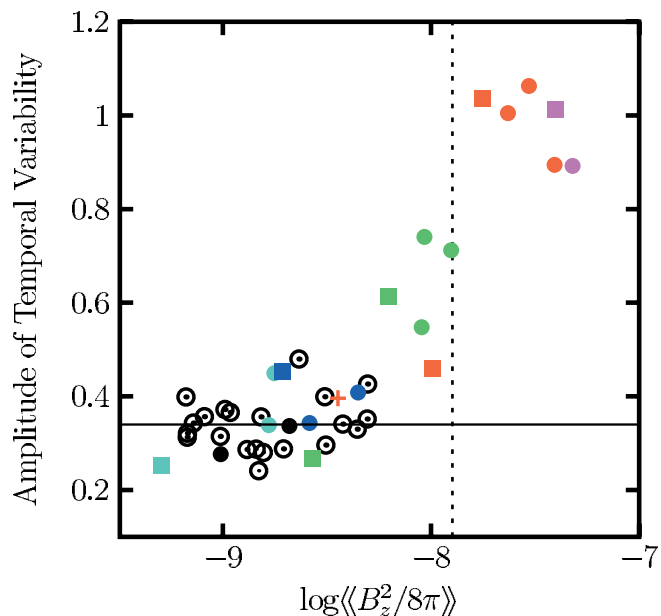

FIG. 14.—Amplitude of temporal variability in the Maxwell stress as a function of the vertical magnetic energy. The amplitude is the time dispersion of the stress normalized by the time-averaged stress. Open circles are from the zero net flux B_z models listed in Table 1. Colored symbols are from uniform B_z models, with meanings as in Fig. 6. The horizontal solid line shows the average, 0.34, among the zero net flux runs. The vertical dotted line indicates where the rms of the MRI wavelength $\langle\langle \lambda_{\rm MRI}^2 \rangle\rangle^{1/2}$ is equal to the vertical size of the computational domain L_z. When the magnetic field in the nonlinear regime is strong enough that $\langle\langle \lambda_{\rm MRI}^2 \rangle\rangle^{1/2} \sim L_z$, the amplitude of time variations is of order unity.
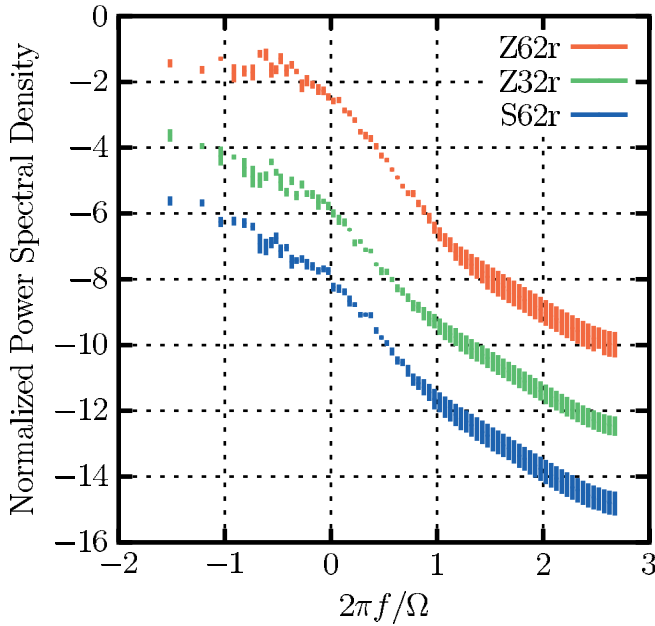
Fig. 15.—Normalized power spectral density for models Z62r (strong uniform field), Z32r (weak uniform field), and S62r (zero net flux). The amplitude is normalized by the squared time average of the stress. The spectra of Z32r and S62r are divided by 10^2 and 10^4, respectively. Each spectrum is the average of eight spectra calculated from eight segments in the history data for each model. The error bars are the standard errors obtained from these eight spectra. The power-law indexes of the spectra are listed in Table 5.

The PSDs of the weak uniform field (Z32r) and zero net flux (S62r) models are quite similar, as are the amplitudes of the time variability (Fig. 14). The strong uniform field model (Z62r) exhibits large time variations with quasi-periodic spike-shaped excursions. The PSD of this model has a steeper slope near the orbital frequency than the other models. The power-law indexes p (PSD $\propto f^{-p}$) of the spectra are listed in Table 5. Because the spectra are not well fitted by single power laws, the indexes are calculated for three different frequency ranges. The indexes for the ideal MHD and anomalous diffusivity models are also listed for purposes of comparison. In all the models, the PSD is steepest in the middle frequency range $0.1 < 2\pi f/\Omega < 1$ and shallowest in the lower frequency range $0.01 < 2\pi f/\Omega < 0.1$.

Basically, the time variation of the stress in the MRI turbulence consists of repeated exponential growth and exponential decay. The PSD of a simple exponential function is flat at low frequencies and proportional to f^{-2} at high frequencies. This feature can be seen at the higher and lower frequencies in the spectra shown in Figure 15. The power-law indexes in the higher range $1 < 2\pi f/\Omega < 10$ are close to 2, and the variation is flattest in the lower range $0.01 < 2\pi f/\Omega < 0.1$. However, the slope is much steeper than $p = 2$ in the middle range $0.1 < 2\pi f/\Omega < 1$. This is because the exponential growth and decay are truncated after finite intervals. The typical period of the spike-shaped variation is a few orbits, and the PSD is enhanced near the corresponding frequency. Armitage & Reynolds (2003) find similar features in the temporal power spectrum of a local annulus in a global disk simulation. X-ray observations of black hole candidates and active galactic nuclei exhibit a power-law decline with a shallower index $p \sim 1$–2 (e.g., Nowak et al. 1999; Papadakis et al. 2002). This suggests again that global disk simulations may be necessary for comparison with observed time variability.

4.1.3. *Growth and Decay Rates of the Stress in Turbulence*

The time variations in stress mostly consist of brief periods of exponential growth and decay. The rates of growth and decay of the Maxwell stress can be estimated approximately by the following method. From the history of the volume-averaged stress $w(t_i)$ sampled at regular intervals, we select local extrema w_{ex}, where $[w(t_{i+1}) - w(t_i)]/[w(t_i) - w(t_{i-1})] < 0$. The extrema occur at times t_{ex}. The rate of change between the jth extremum and the next is calculated by

$$\omega = \frac{\ln w_{\mathrm{ex},j+1} - \ln w_{\mathrm{ex},j}}{t_{\mathrm{ex},j+1} - t_{\mathrm{ex},j}}, \quad (14)$$

where a positive (negative) sign for ω indicates growth (decay). When the time between peaks is short, the change in stress is small. We ignore intervals less than $0.1t_{\mathrm{rot}}$.

Histograms of the growth and decay rates are shown in Figure 16 for models Z62r, Z32r, and S62r. The weak uniform field model (Z32r) and zero net flux model (S62r) have quite similar distributions, symmetric between growth and decay. By contrast, the distribution for model Z62r is obviously asymmetric. As mentioned above, turbulence in models Z32r and S62r is disorganized, and the growth and decay of perturbations in different parts of the simulation volume are uncorrelated. When averaged over the many perturbations present, the stress varies less with time than in each individual perturbation. The histogram peaks at growth rates less than the maximum for the MRI, $\omega_{\mathrm{max}} = 0.75\Omega$. In model Z62r, on the other hand, increases are due to the growth of the domain-filling two-channel flow, and decay happens by nearly simultaneous magnetic reconnection throughout. The mean growth rate 0.23Ω is not much less than the MRI growth rate. The distribution of decay rates shows a tail extending to faster values, suggesting that reconnection rates may differ from one event to another.

The timescale of magnetic reconnection depends on the Alfvén speed. For example, the timescale of the slow reconnection model (Sweet 1958; Parker 1957, 1963) is given by

$$\tau_{\mathrm{rec}} = \frac{L}{v_A}\sqrt{S} = \frac{L^{3/2}}{v_A^{1/2}\eta^{1/2}}, \quad (15)$$

TABLE 5
POWER-LAW INDEXES OF POWER SPECTRAL DENSITY

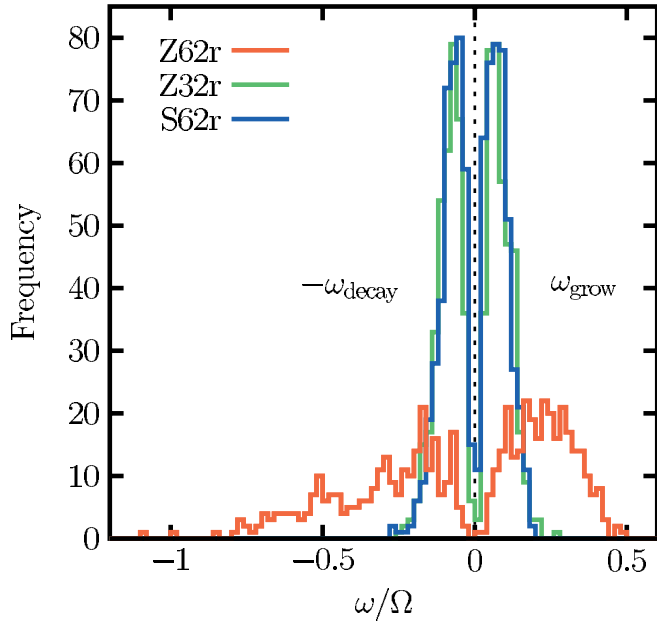| MODEL	FREQUENCY RANGE ($2\pi f/\Omega$)		
	0.1–1	1–10	10–100
Strong Uniform Field			
Z62	1.31	4.41	2.16
Z62r..........	1.00	4.14	2.35
Z62a	0.54	4.01	2.06
Weak Uniform Field			
Z32	1.80	3.66	2.07
Z32r..........	1.46	3.58	2.04
Z32a	1.66	3.66	2.05
Zero Net Flux			
S62	1.83	4.12	2.11
S62r..........	1.81	3.81	2.08
S62a..........	1.70	3.33	2.02

FIG. 16.—Histograms of growth and decay rates in models Z62r (strong uniform field), Z32r (weak uniform field), and S62r (zero net flux). The rates are defined by eq. (14). The distribution is asymmetric in model Z62r and symmetric in the other two models.

where L is the size of a reconnection region and $S = Lv_A/\eta$. If $\omega_{\rm decay} \sim \tau_{\rm rec}^{-1}$, then decay will be faster when the Alfvén speed is faster. Figure 17 shows the growth (circles) and decay rates (squares) for model Z62r as a function of the Maxwell stress. Time intervals with larger jumps in the stress, $\left| \ln w_{\mathrm{ex},j+1} - \ln w_{\mathrm{ex},j} \right| > 1$, are selected for this figure. The magnetic energy is proportional to the Maxwell stress, so that the horizontal axis also indicates the amplitude of the magnetic energy. The growth rate is independent of the magnetic stress, while the decay rate increases with magnetic stress and energy. Similar relations occur in the anomalous diffusivity (Z62a) and ideal MHD models (Z62). The Alfvén speed is $v_A = (2w_M/f\rho_0)^{1/2}$, where $f \equiv w_M/P_{\rm mag} \approx 0.5$ is the ratio of the Maxwell stress to the magnetic pressure (Table 4). If the field decays as a result of reconnection at a rate $\omega_{\rm rec} \equiv \tau_{\rm rec}^{-1} = L^{-3/2}v_A^{1/2}\eta^{1/2}$, then

$$\frac{\omega_{\rm rec}}{\Omega} = \frac{v_A^{1/2}\eta^{1/2}}{L^{3/2}\Omega} \approx \left(\frac{f}{0.5}\right)^{-1/4}\left(\frac{L}{0.2}\right)^{-3/2}\left(\frac{w_M}{P_0}\right)^{1/4} \quad (16)$$

for model Z62r ($P_0 = 1.25 \times 10^{-5}$, $\eta = 10^{-6}$, and $\Omega = 10^{-3}$). The relation given by equation (16) is shown by a dot-dashed line in the figure. Of course, this interpretation may be too simplified to compare with the simulation results because the Sweet-Parker picture is based on a steady structure in the reconnection region. In MRI-driven turbulence, reconnection continues at most a few orbits because the supply of magnetic flux entering the diffusion region is limited. Reconnection in this situation may be unsteady. It is evident that magnetic reconnection is a key process in determining the saturation level of the MRI turbulence. Magnetic reconnection also makes a major contribution to magnetic energy release in global disk simulations (Machida & Matsumoto 2003). Understanding nonsteady magnetic reconnection may be important for future progress.

4.2. Origin of the Pressure Dependence

The magnetic energy in the saturated turbulence is determined by a balance between field enhancement by the MRI and dissipation through magnetic reconnection. The linear growth rate of the MRI is independent of the gas pressure if the magnetic pressure is much smaller than the gas pressure, as it is in the turbulence. Thus, it is quite natural to expect that the gas pressure dependence of the stress may arise from a pressure dependence in the rate of dissipation by magnetic reconnection. The effects of gas pressure on magnetic reconnection are examined by Ugai & Kondoh (2001), using two-dimensional MHD simulations with an anomalous resistivity. Conditions differ from those we considered in that magnetic pressure exceeds gas pressure. Smaller gas pressures lead to thinner current sheets and more drastic reconnection. The gas pressure also affects reconnection in laboratory experiments by Ji et al. (1998). High gas pressures downstream from the diffusion region substantially reduce the outflow and thus the reconnection rate. Overall, the results of these simulations and experiments are consistent with a picture in which higher gas pressures lead to slower reconnection of magnetic fields.

The fluctuation-dissipation relation, equation (9), links the rate of change of thermal energy to the stress in the nonlinear regime. If the limiting process in the energy change is reconnection, the left-hand side of equation (9) is approximately $dE_{\rm th}/dt \sim E_{\rm th}/\tau_{\rm rec}$, and the saturated stress is proportional to $P/\tau_{\rm rec}$. The stress may vary overall with $P^{1/4}$, as in the zero net flux B_z models, if the reconnection timescale is proportional to $P^{3/4}$. For example, if the size of the reconnection region is proportional to the pressure scale height ($L \propto c_s/\Omega$), then $\tau_{\rm rec} \propto L^{3/2} \propto P^{3/4}$. The interpretation discussed here is qualitatively consistent with our numerical results. For further quantitative discussion, it may be necessary to understand the effects of gas pressure on nonsteady magnetic reconnection.
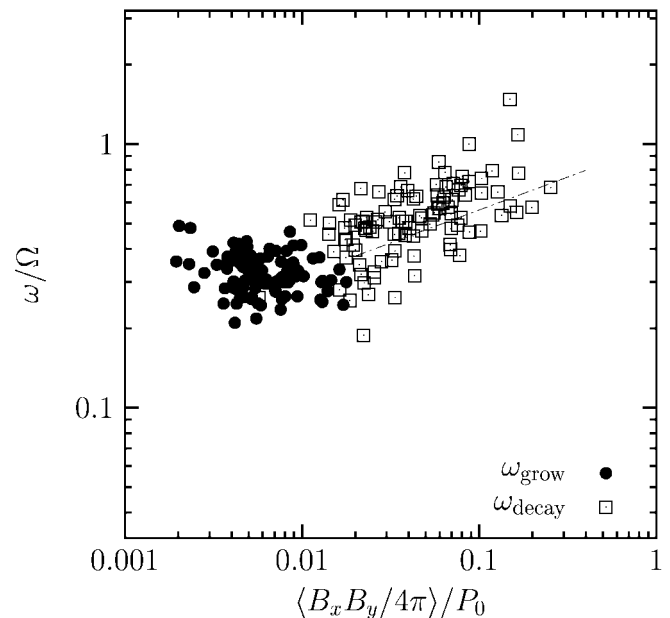

FIG. 17.—Growth (circles) and decay (squares) rates in model Z62r as functions of the magnetic stress. For this figure, data are taken only from time intervals with larger changes in the stress, $\left| \ln w_{\mathrm{ex},j+1} - \ln w_{\mathrm{ex},j} \right| > 1$. The growth rate is almost independent of the magnetic stress, but the decay rate is larger when the magnetic stress and magnetic energy are larger. The dot-dashed line indicates the decay rate estimated from a simple model based on Sweet-Parker type reconnection.

5. SUMMARY

We investigate the saturation level of the MRI using three-dimensional MHD simulations. To simplify the problem, the local shearing box approximation is adopted and the vertical component of gravity is ignored. The dependence of the saturation level on the physical quantities is scrutinized, with special attention to effects of gas pressure. The gas pressure increases with time in adiabatic calculations, and the increase affects the long-term evolution of the saturation level. This feature is carefully taken into account in the analysis of the gas pressure dependence. The main results are summarized below.

1. A power-law relation between the saturation amplitude of the Maxwell stress and the gas pressure in the nonlinear regime is derived from all the models performed in this paper. The power-law index is small ($q = \frac{1}{4} - \frac{1}{6}$) and varies slightly with the geometry of the magnetic field.

2. For the zero net flux models, the power-law index is about $\frac{1}{4}$ and the saturation level is independent of the initial gas pressure, the magnetic field strength, and the equation of state. However, if the MRI wavelength is not resolved by at least six grid zones, the saturation level is affected greatly by numerical dissipation.

3. For the models with a uniform vertical initial field, the power-law index in the pressure-stress relation is smaller than that in the zero net flux models. The saturation level is higher for larger vertical magnetic fluxes, but there are upper and lower limits on the saturation level depending on the strength of the uniform field.

4. Similar pressure-stress relations are obtained in ideal MHD calculations and resistive MHD models with magnetic Reynolds numbers greater than about 10. There is no clear difference in saturation level between models with a uniform diffusivity and an anomalous diffusivity.

5. There exist many characteristic ratios among the quantities in the MRI turbulence. The ratios are independent of initial conditions, including the strength and geometry of the magnetic field and the gas pressure. The perturbed magnetic and kinetic energies are maintained near equipartition.

6. The amplitude of time variability in the Maxwell stress is characterized by the ratio of the magnetic pressure to the gas pressure in the nonlinear regime. The power spectral density of the temporal variability generally has a steep slope around the frequency corresponding to a few orbits.

The gas pressure dependence of the saturation level may originate in the process of magnetic reconnection. The gain side of the magnetic energy balance is unlikely to depend on gas pressure, since the MRI linear growth rate is independent of the pressure when plasma β exceeds unity. Although there is some qualitative evidence supporting an idea that higher gas pressures reduce reconnection rates, a deeper understanding of magnetic reconnection is necessary for a quantitative discussion of the saturation mechanism of the MRI.

The final goal of this work is to derive a predictor function for the saturation level of the MRI. For this purpose, we must determine how the saturation level depends on all the physical quantities. For example, we have studied the gas pressure dependence using the local shearing box approximation, with the height of the box independent of the gas pressure. In real accretion disks, however, the scale height of the disk varies according to the pressure. Before proceeding to derive a saturation predictor and to examine the similarities and differences between the α-prescription and numerical results, the effects of changes in disk thickness must be considered. The effects of the other parameters, as well as a final form of the predictor function, will be discussed in a subsequent paper.

REFERENCES

Armitage, P. J., & Reynolds, C. S. 2003, MNRAS, 341, 1041
Balbus, S. A., & Hawley, J. F. 1991, ApJ, 376, 214
———. 1998, Rev. Mod. Phys., 70, 1
Balbus, S. A., & Papaloizou, J. C. 1999, ApJ, 521, 650
Blaes, O. M., & Balbus, S. A. 1994, ApJ, 421, 163
Brandenburg, A., Nordlund, Å., Stein, R. F., & Torkelsson, U. 1995, ApJ, 446, 741
Chandrasekhar, S. 1961, Hydrodynamic and Hydromagnetic Stability (New York: Dover)
Colella, P., & Woodward, P. R. 1984, J. Comput. Phys., 54, 174
Evans, C. R., & Hawley, J. F. 1988, ApJ, 332, 659
Fleming, T. P., Stone, J. M., & Hawley, J. F. 2000, ApJ, 530, 464
Goodman, J., & Xu, G. 1994, ApJ, 432, 213
Hawley, J. F., Gammie, C. F., & Balbus, S. A. 1995, ApJ, 440, 742
———. 1996, ApJ, 464, 690
Igumenshchev, I. V., Narayan, R., & Abramowicz, M. A. 2003, ApJ, 592, 1042
Ji, H., Yamada, M., Hsu, S., & Kulsrud, R. 1998, Phys. Rev. Lett., 80, 3256
Kawaguchi, T., Mineshige, S., Machida, M., Matsumoto, R., & Shibata, K. 2000, PASJ, 52, L1
Kim, W.-T., & Ostriker, E. C. 2000, ApJ, 540, 372
Landau, L. D., & Lifshitz, E. M. 1959, Fluid Mechanics (London: Pergamon)
Machida, M., & Matsumoto, R. 2003, ApJ, 585, 429
Matsumoto, R., & Tajima, T. 1995, ApJ, 445, 767
Nowak, M. A., Vaughan, B. A., Wilms, J., Dove, J. B., & Begelman, M. C. 1999, ApJ, 510, 874
Papadakis, I. E., Brinkmann, W., Negoro, H., & Gliozzi, M. 2002, A&A, 382, L1
Parker, E. N. 1957, J. Geophys. Res., 62, 509
———. 1963, ApJS, 8, 177
Sano, T. 1998, Ph.D. thesis, Univ. Tokyo
Sano, T., & Inutsuka, S. 2001, ApJ, 561, L179
Sano, T., Inutsuka, S., & Miyama, S. M. 1998, ApJ, 506, L57
Sano, T., & Miyama, S. M. 1999, ApJ, 515, 776
Sano, T., & Stone, J. M. 2002a, ApJ, 570, 314
———. 2002b, ApJ, 577, 534
Shakura, N. I., & Sunyaev, R. A. 1973, A&A, 24, 337
Stone, J. M., Hawley, J. F., Gammie, C. F., & Balbus, S. A. 1996, ApJ, 463, 656
Stone, J. M., & Norman, M. L. 1992, ApJS, 80, 791
Sweet, P. A. 1958, in Electromagnetic Phenomena in Cosmical Physics, ed. B. Lehnert (New York: Cambridge Univ. Press), 123
Turner, N. J., Stone, J. M., Krolik, J. H., & Sano, T. 2003, ApJ, 593, 992
Turner, N. J., Stone, J. M., & Sano, T. 2002, ApJ, 566, 148
Ugai, M., & Kondoh, K. 2001, Phys. Plasmas, 8, 1545
van Leer, B. 1979, J. Comput. Phys., 32, 101
Winters, W. F., Balbus, S. A., & Hawley, J. F. 2003, MNRAS, 340, 519
Yokoyama, T., & Shibata, K. 1994, ApJ, 436, L197